

Neural Wavelet-domain Diffusion for 3D Shape Generation, Inversion, and Manipulation

JINGYU HU*, KA-HEI HUI*, ZHENGZHE LIU, The Chinese University of Hong Kong, HK SAR, China

RUIHUI LI, Hunan University, HK SAR, China

CHI-WING FU, The Chinese University of Hong Kong, HK SAR, China

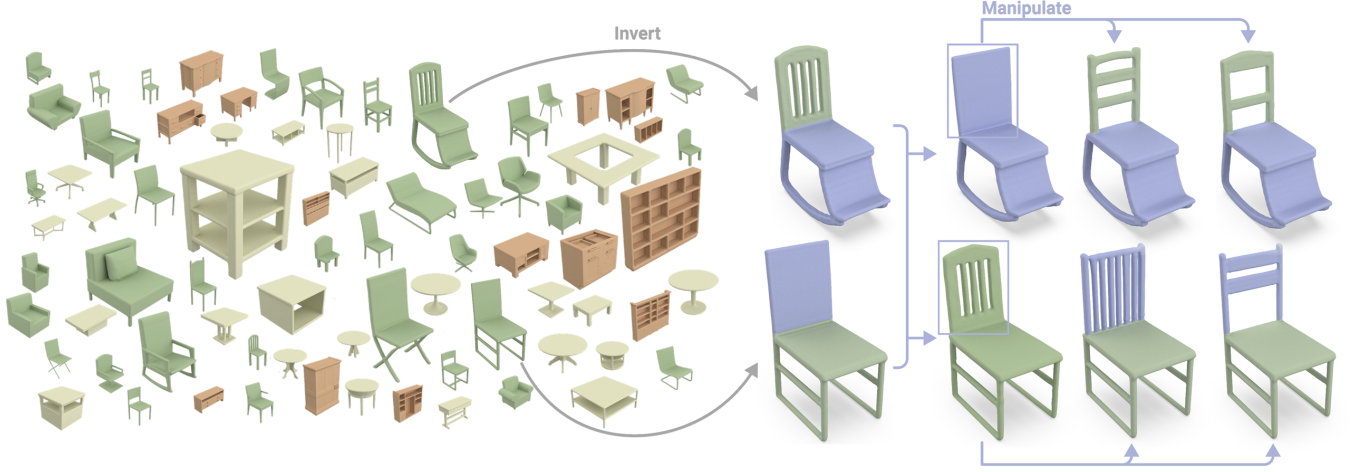


Fig. 1. Our new framework is able to generate diverse and realistic 3D shapes that exhibit complex structures and topology, fine details, and clean surfaces, without obvious artifacts (left). Also, we can encode shapes and invert (reconstruct) them from their codes with high fidelity (middle). Further, we may manipulate shapes in a region-aware manner and generate new shapes by composing/re-generating parts from existing or randomly-generated shapes (right).

This paper presents a new approach for 3D shape generation, inversion, and manipulation, through a direct generative modeling on a continuous implicit representation in wavelet domain. Specifically, we propose a *compact wavelet representation* with a pair of coarse and detail coefficient volumes to implicitly represent 3D shapes via truncated signed distance functions and multi-scale biorthogonal wavelets. Then, we design a pair of neural networks: a diffusion-based *generator* to produce diverse shapes in the form of the coarse coefficient volumes and a *detail predictor* to produce compatible detail coefficient volumes for introducing fine structures and details. Further, we may jointly train an *encoder network* to learn a latent space for inverting shapes, allowing us to enable a rich variety of whole-shape and region-aware shape manipulations. Both quantitative and qualitative experimental results manifest the compelling shape generation, inversion, and manipulation capabilities of our approach over the state-of-the-art methods.

CCS Concepts: • **Computing methodologies** → **Shape analysis; Neural networks; Mesh models.**

Additional Key Words and Phrases: shape generation, shape manipulation, diffusion model, wavelet representation

1 INTRODUCTION

Generative modeling of 3D shapes enables rapid creation of 3D contents, enriching extensive applications across graphics, vision, and VR/AR. With the emerging large-scale 3D datasets [Chang et al. 2015], data-driven shape generation has gained increasing attention. However, it is still very challenging to learn to generate 3D shapes that are diverse, realistic, and novel, while promoting controllability on part- or region-aware shape manipulations with high fidelity.

Existing shape generation models are developed mainly for voxels [Girdhar et al. 2016; Yang et al. 2018; Zhu et al. 2017], point clouds [Achlioptas et al. 2018; Fan et al. 2017; Jiang et al. 2018], and meshes [Groueix et al. 2018; Smith et al. 2019; Tang et al. 2019; Wang et al. 2018]. Typically, these representations cannot handle high resolutions or irregular topology, thus unlikely producing high-fidelity results. In contrast, implicit functions [Chen and Zhang 2019; Mescheder et al. 2019; Park et al. 2019] show improved performance in surface reconstructions. By representing a 3D shape as a level set of discrete volume or a continuous field, we can flexibly extract a mesh object of arbitrary topology at desired resolution.

Existing generative models such as GANs and normalizing flows have shown great success in generating point clouds and voxels. Yet, they cannot effectively generate implicit functions. To represent a surface in 3D, a large number of point samples are required, even though many nearby samples are redundant. Taking the occupancy field for instance, only regions near the surface have varying data values, yet we need huge efforts to encode samples in constant and smoothly-varying regions. Such representation non-compactness and redundancy demands a huge computational cost and hinders the learning efficiency on implicit surfaces.

To address these challenges, some methods attempt to sample in a pre-trained latent space built on the reconstruction task [Chen and Zhang 2019; Mescheder et al. 2019] or convert the generated implicit into point clouds or voxels for adversarial learning [Kleineberg et al. 2020; Luo et al. 2021]. However, these regularizations can only be indirectly applied to the generated implicit functions, so they

* joint first authors.

are not able to ensure the generation of realistic objects. Hence, the visual quality of the generated shapes often shows a significant gap, as compared with the 3D reconstruction results, and the diversity of their generated shapes is also quite limited.

Further, to promote controllability in whole-shape or part-wise manipulation on implicit shapes is challenging. Some works encode implicit shapes into latent codes and perform shape manipulation by modifying the latent codes [Chen and Zhang 2019; Mescheder et al. 2019; Park et al. 2019]. To achieve part-wise controllability, some methods [Hao et al. 2020; Hertz et al. 2022] learn to decompose implicit shapes into a set of templates and manipulate corresponding templates of specific parts. Yet, these methods struggle to invert (implicitly encode then reconstruct) shapes faithfully due to the redundancy in the sample-based implicit representation, which further hinders the shape manipulation quality. Recently, [Lin et al. 2022] propose a method to manipulate implicit shapes by introducing extra part annotations, which enhance the quality of shape inversion and manipulation. Yet, preparing part annotations on 3D shapes is tedious and costly. Also, instead of refining the latent code at testing, their method overfits each unseen shape and the process is time-consuming, *i.e.*, around 25 minutes per shape.

This work introduces a new approach for 3D shape generation, inversion, and manipulation, enabling a direct generative modeling on a continuous implicit representation in the compact wavelet frequency domain. Overall, we have six key contributions: (i) a compact wavelet representation (a pair of coarse and detail coefficient volumes) based on the biorthogonal wavelets and truncated signed distance field to implicitly encode 3D shapes, facilitating effective learning for shape generation and inversion; (ii) a generator network formulated based on the diffusion probabilistic model [Sohl-Dickstein et al. 2015] to produce coarse coefficient volumes from random noise samples, promoting the generation of diverse and novel shapes; (iii) a detail predictor network, formulated to produce compatible detail coefficients to enhance the generation of fine details; (iv) an encoder network, jointly trained with the generator to build a latent space for supporting shape inversion and manipulation; (v) a shape-guided refinement scheme to enhance the shape inversion quality; and (vi) region-aware manipulation for implicitly editing object regions without additional part annotations.

In this work, with the generator and detail predictor, we can flexibly generate diverse and realistic shapes that are not necessarily the same as the training shapes. Further with the encoder network, we can embed a shape, not necessarily in the training set, into our compact latent space for shape inversion and manipulation. As Figure 1 shows, our generated shapes exhibit diverse topology, clean surfaces, sharp boundaries, and fine details, without obvious artifacts. Fine details such as curved/thin beams, small pulleys, and complex cabinets are very challenging for the existing 3D generation approaches to synthesize. Besides, our method can faithfully invert and reconstruct randomly-generated shapes, as shown in the middle of Figure 1. Further, we support a rich variety of shape manipulations, *e.g.*, composing/re-generating parts from existing or randomly-generated shapes; see the right of Figure 1.

This work extends [Hui et al. 2022], which was presented very recently in a conference. The previous work [Hui et al. 2022] focuses

mainly on unconditional 3D shape generation. In this extended version, we first expand [Hui et al. 2022] with an encoder network and the shape-guided refinement scheme to build a latent space, enabling us to faithfully invert 3D shapes. Besides, we design the region-aware manipulation procedure to support applications beyond shape interpolation, *e.g.*, part replacement, part-wise interpolation, and part-wise re-generation. Further, by utilizing the compact latent space, we explore the potential of our method for reconstructing implicit shapes from point clouds or images. Also, we perform various new experiments to evaluate our framework on shape inversion and shape manipulation, and include more comparisons, including GET3D [Gao et al. 2022], a very recent work on 3D shape generation. Both quantitative and qualitative experimental results manifest the superiority of our method on 3D generation, inversion, and manipulation over the state-of-the-art methods.

2 RELATED WORK

3D reconstruction via implicit function. Recently, many methods leverage the flexibility of implicit surface for 3D reconstructions from voxels [Chen and Zhang 2019; Mescheder et al. 2019], complete/partial point clouds [Liu et al. 2021; Park et al. 2019; Yan et al. 2022], and RGB images [Li and Zhang 2021; Tang et al. 2021; Xu et al. 2019, 2020]. On the other hand, besides ground-truth field values, various supervisions have been explored to train the generation of implicit surfaces, *e.g.*, multi-view images [Liu et al. 2019; Niemeyer et al. 2020] and unoriented point clouds [Atzmon and Lipman 2020; Gropp et al. 2020; Zhao et al. 2021]. Yet, the task of 3D reconstruction focuses mainly on synthesizing a high-quality 3D shape that best matches the input. So, it is fundamentally very different from the task of 3D shape generation, which aims to learn the shape distribution of a given set of shapes for generating diverse, high-quality, and possibly novel shapes accordingly.

3D shape generation via implicit function. Unlike the 3D reconstruction task, 3D shape generation has no fixed ground truth to supervise the generation of each shape sample. Exploring efficient guidance for implicit surface generation is still an open problem. Some works attempt to use the reconstruction task to first learn a latent embedding [Chen and Zhang 2019; Hao et al. 2020; Ibing et al. 2021; Mescheder et al. 2019] then generate new shapes by decoding codes sampled from the learned latent space. Recently, [Hertz et al. 2022] learn a latent space with a Gaussian-mixture-based auto-decoder for shape generation and manipulation. Though these approaches ensure a simple training process, the generated shapes have limited diversity restricted by the pre-trained shape space. Some other works attempt to convert implicit surfaces to some other representations, *e.g.*, voxels [Kleineberg et al. 2020; Zheng et al. 2022], point cloud [Kleineberg et al. 2020], and mesh [Luo et al. 2021], for applying adversarial training. Yet, the conversion inevitably leads to information loss in the generated implicit surfaces, thus reducing the training efficiency and generation quality.

In this work, we propose a compact wavelet representation for modeling the implicit surface and learn to synthesize it with a diffusion model. By this means, we can effectively learn to generate the implicit representation without a pre-trained latent space and a representation conversion. The results in Section 5.1 also show

that our new approach is capable of producing diversified shapes of high visual quality, exceeding the state-of-the-art methods.

3D shape generation via other representations. [Smith and Meger 2017; Wu et al. 2016] explore voxels, a natural grid-based extension of 2D image. Yet, the methods learn mainly coarse structures and fail to produce fine details due to memory restriction. Some other methods explore point clouds via GAN [Gal et al. 2020; Hui et al. 2020; Li et al. 2021], flow-based models [Cai et al. 2020; Kim et al. 2020], and diffusion models [Zhou et al. 2021]. Due to the discrete nature of point clouds, 3D meshes reconstructed from them often contain artifacts. This work focuses on implicit surface generation, aiming at generating high-quality and diverse meshes with fine details and overcoming the limitations of the existing representations.

3D shape inversion & manipulation via implicit function. The inversion task was first proposed for 2D images, aiming at embedding a given image, not necessarily in the training set, into a trained model’s latent space [Abdal et al. 2021; Bau et al. 2019; Tewari et al. 2020; Tov et al. 2021; Xia et al. 2022; Zhu et al. 2016], so that we can perform semantic manipulations on the image and reconstruct a modified version of it from the manipulated latent code. 3D shape inversion is a relatively new topic. So far, research works mainly explored the following 3D representations, *e.g.*, point clouds [Zhang et al. 2021], voxels [Wu et al. 2016], and part-annotated bounding boxes or point clouds [Li et al. 2017b; Mo et al. 2019].

The existing inversion approaches for implicit representations can be divided into two categories: (i) leveraging an auto-encoder framework to map the given shape to the latent space [Chen and Zhang 2019; Genova et al. 2020; Mescheder et al. 2019] and (ii) optimizing the latent code at test time without using an additional encoder [Hao et al. 2020; Hertz et al. 2022; Lin et al. 2022; Park et al. 2019]. We combine their strengths by initializing the latent code through an encoder network and further refining the code in a shape-guided manner; see Section 5.2 for the experimental results, which demonstrate the compelling performance of our method.

More importantly, 3D shape inversion enables user manipulations on existing shapes in the compact latent space. Some recent works [Gal et al. 2020; Hui* et al. 2022; Li et al. 2021; Mo et al. 2019; Wei et al. 2020] explore shape manipulation in the latent space via explicit 3D representations. Yet, manipulation is still challenging for neural implicit representations. First, some existing works [Chen and Zhang 2019; Mescheder et al. 2019; Park et al. 2019] lack part-level awareness in the manipulation. Second, the inversion quality can be severely limited by the shape representative capability of their models [Hao et al. 2020; Hertz et al. 2022]. A very recent work [Lin et al. 2022] enables part-aware manipulation with good quality but it requires extra part annotations, which are costly to prepare. In this work, we propose a rich variety of region-aware manipulations, besides whole-shape interpolation, without requiring part-level annotations; see Section 5.3 for the high-fidelity manipulated shapes that can be generated using our new approach.

Multi-scale neural implicit representation. This work also relates to multi-scale representations, so we discuss some 3D deep learning works in this area. [Chen et al. 2021; Chibane et al. 2020; Liu et al. 2020; Martel et al. 2021; Takikawa et al. 2021] predict multi-scale latent codes in an adaptive octree to improve the reconstruction

quality and inference efficiency. [Fathony et al. 2020] propose a band-limited network to obtain a multi-scale representation by restricting the frequency magnitude of the basis functions. Recently, [Sara-gadam et al. 2022] adopt the Laplacian pyramid to extract multi-scale coefficients for multiple neural networks. Unlike our work, this work overfits each input object with an individual representation for efficient storage and rendering. In contrast to our work on shape generation, the above methods focus on improving 3D reconstruction performance by separately handling features at different levels. In our work, we adopt a multi-scale implicit representation based on wavelets (motivated by [Velho et al. 1994]) to build a compact representation for high-quality shape generation.

Diffusion-based models. [Ho et al. 2020; Nichol and Dhariwal 2021; Sohl-Dickstein et al. 2015; Song et al. 2020] recently show top performance in image generation, surpassing GAN-based models [Dhariwal and Nichol 2021]. Recently, [Luo and Hu 2021; Zhou et al. 2021] adopt diffusion models for point cloud generation. Yet, they fail to generate smooth surfaces and complex structures, as point clouds contain only discrete samples. Distinctively, we adopt a compact representation based on wavelets to model the continuous signed distance field in our diffusion model, promoting 3D shape representation with diverse structures and fine details.

3 OVERVIEW

As shown in Figure 2, our approach has the following procedures:

(i) *Data preparation* is a one-time process for preparing a compact wavelet representation from each input shape; see Figure 2(a). For each shape, we sample a signed distance field (SDF) and truncate its distance values to avoid redundant information. Then, we transform the truncated SDF to the wavelet domain to produce a series of multi-scale coefficient volumes. Importantly, we take a *pair of coarse and detail coefficient volumes* at the same scale as our compact wavelet representation for implicitly encoding the input shape.

(ii) *Shape learning* aims to train a pair of neural networks to learn the 3D shape distribution from the coarse and detail coefficient volumes; see Figure 2(b). First, we adopt the denoising diffusion probabilistic model [Sohl-Dickstein et al. 2015] to formulate and train the *generator network* to learn to iteratively refine a random noise sample for generating diverse 3D shapes in the form of the coarse coefficient volume. Second, we design and train the *detail predictor network* to learn to produce the detail coefficient volume from the coarse coefficient volume for introducing further details in our generated shapes. Besides, we jointly train an additional encoder with the generator for mapping the coarse coefficient volume to a compact latent code. By doing so, the latent code can serve as a controllable condition in the generation, enabling applications such as shape inversion and manipulation; see (iv) below.

(iii) *Shape generation* employs the two trained networks to generate 3D shapes; see Figure 2(c). Starting from a random Gaussian noise sample, we first use the trained generator to produce the coarse coefficient volume then the detail predictor to produce an associated detail coefficient volume. After that, we can perform an

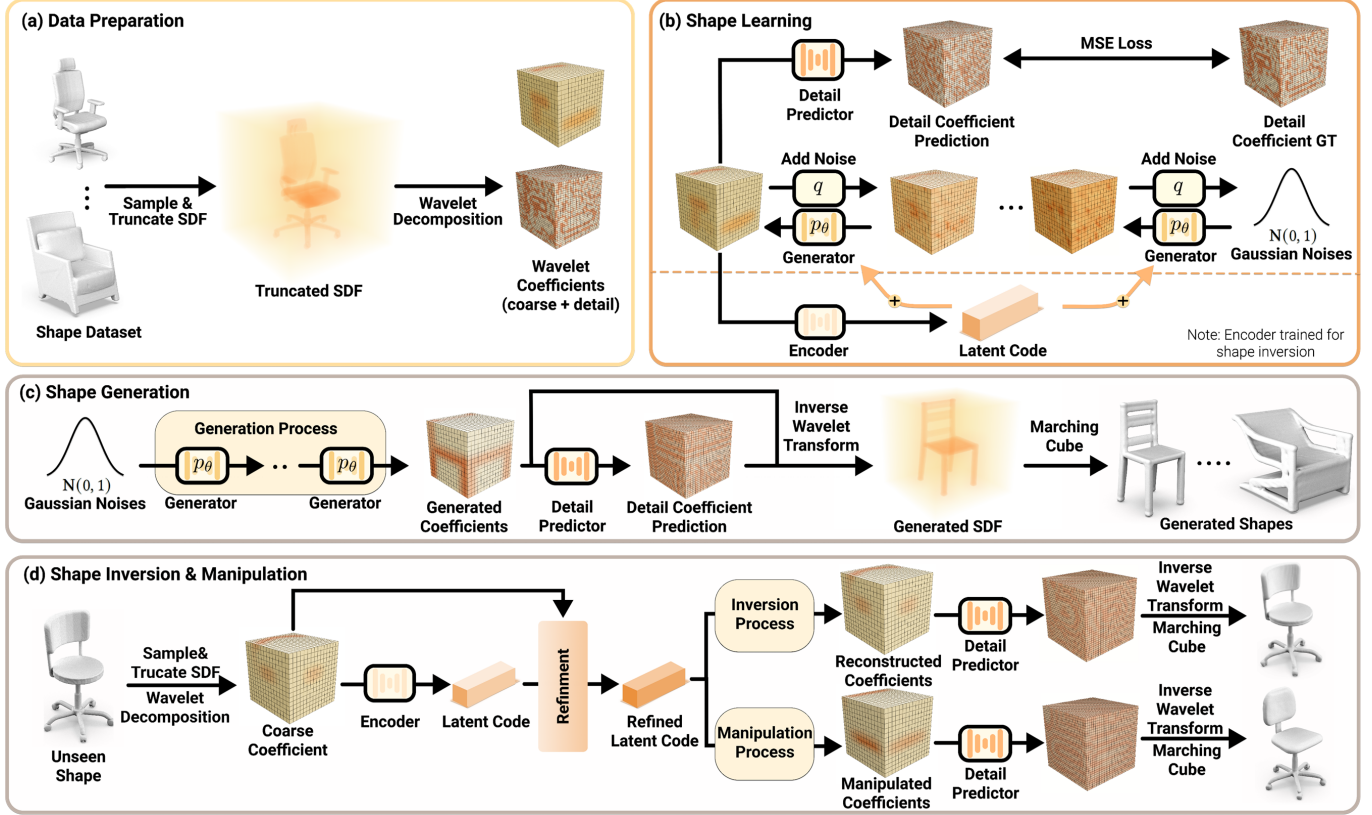


Fig. 2. Overview of our approach. (a) *Data preparation* builds a compact wavelet representation (a pair of coarse and detail coefficient volumes) for each input shape using a truncated signed distance field and a multi-scale wavelet decomposition. (b) *Shape learning* trains the generator network to produce coarse coefficient volumes from random noise samples and trains the detail predictor network to produce detail coefficient volumes from coarse coefficient volumes. Further, an encoder is jointly trained with the generator to build a compact latent space for shape inversion and manipulation. (c) *Shape generation* employs the trained generator to produce a coarse coefficient volume and then the trained detail predictor to further predict a compatible detail coefficient volume, followed by an inverse wavelet transform and marching cube, to generate the output 3D shape. (d) *Shape inversion & manipulation* employ the trained encoder to map a given shape to our compact latent space, then refine the latent code to enable faithful reconstruction and high-quality shape manipulation.

inverse wavelet transform, followed by the marching cube operator [Lorensen and Cline 1987], to generate the output 3D shape.

(iv) *Shape inversion & manipulation* aim to embed a given shape in the generator’s latent space, such that we may manipulate the shape and reconstruct it; see Figure 2(d). To invert a shape, we follow procedures (i) & (ii) to sample a truncated signed distance field (TSDF) from the shape, transform it to the wavelet domain, and derive its latent code using the encoder jointly trained in procedure (ii). Then, we enhance the correspondence between the shape and the latent code by refining the latent code via a back propagation with the frozen generator and encoder. Further, we perform manipulation and reconstruction by feeding the derived (or manipulated) latent code as a condition on the generator to reconstruct the final shape. Also, by utilizing the trained latent space, we can perform various region-aware manipulations on the given shape.

4 METHOD

4.1 Compact Wavelet Representation

Preparing a compact wavelet representation of a given 3D shape (see Figure 2(a)) involves the following two steps: (i) implicitly represent the shape using a signed distance field (SDF); and (ii) decompose the implicit representation via wavelet transform into coefficient volumes, each encoding a specific scale of the shape.

In the first step, we scale each shape to fit $[-0.9, +0.9]^3$ and sample an SDF of resolution 256^3 to implicitly represent the shape. Importantly, we truncate the distance p in the SDF to $[-0.1, +0.1]$, so regions not close to the object surface are clipped to a constant. We denote the truncated signed distance field (TSDF) for the i -th shape in training set as S_i . Using S_i , we can significantly reduce the shape representation redundancy, such that the shape learning process can focus better on the shape structures and fine details.

The second step is a multi-scale wavelet decomposition [Daubechies 1990; Mallat 1989; Velho et al. 1994] on the TSDF. Here, we decompose S_i into a high-frequency detail coefficient volume and a low-frequency coarse coefficient volume, which is roughly a compressed

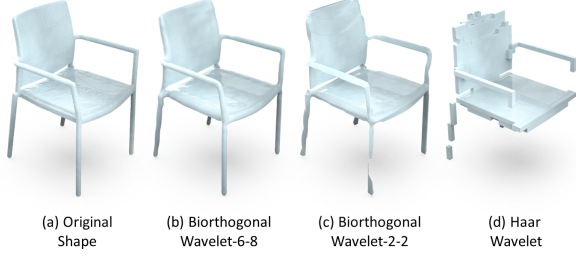


Fig. 3. Reconstructions with different wavelet filters. (a) An input shape from ShapeNet. (b,c) Reconstructions from the $J=3$ coefficient volumes with biorthogonal wavelets. The two numbers mean the vanishing moment of the synthesis and analysis wavelets. (d) Reconstruction with the Haar wavelet.

version of S_i . We repeat this process J times on the coarse coefficient volume of each scale, decomposing S_i into a series of multi-level coefficient volumes. We denote the coarse and detail coefficient volumes at the j -th step (scale) as C_i^j and D_i^j , respectively, where $j = \{1, \dots, J\}$. The representation is lossless, meaning that the extracted coefficient volumes together can faithfully reconstruct the original TSDF via a series of inverse wavelet transforms.

There are three important considerations in the data preparation. First, multi-scale decomposition can effectively separate rich structures, fine details, and noise in the TSDF. Empirically, we evaluate the reconstruction error on the TSDF by masking out all higher-scale detail coefficients and reconstructing S_i only from the coefficients at scale $J = 3$, i.e., C_i^3 and D_i^3 . We found that the reconstructed TSDF values have relatively small changes from the originals (only 2.8% in magnitude), even without 97% of the coefficients for the Chair category in ShapeNet [Chang et al. 2015]. Comparing Figures 3 (a) vs. (b), we can see that reconstructing only from the coarse scale of $J = 3$ already well retains the chair’s structure. Motivated by this observation, we propose to construct the compact wavelet representation at a coarse scale ($J = 3$) and drop other detail coefficient volumes, i.e., D_i^1 and D_i^2 , for efficient shape learning. See supplementary material Section I for more details on the wavelet decomposition.

Second, we need a suitable wavelet filter. While Haar wavelet is a popular choice due to its simplicity, using it to encode smooth and continuous signals such as the SDF may introduce serious voxelization artifacts, see, e.g., Figure 3(d). In this work, we propose to adopt the biorthogonal wavelets [Cohen 1992], since it enables a more smooth decomposition of the TSDF. Specifically, we tried different settings in the biorthogonal wavelets and chose to use high vanishing moments: six for the synthesis filter and eight for the analysis filter; see Figures 3(b) vs. (c). Also, instead of storing the detail coefficient volumes with seven channels, as in traditional wavelet decomposition, we follow [Velho et al. 1994] to efficiently compute it as the difference between the inverse transformed C_i^j and C_i^{j-1} in a Laplacian pyramid style. Hence, the detail coefficient volume has a higher resolution than the coarser one, but both have much lower resolution than the original TSDF volume (256^3).

Last, it is important to truncate the SDF before constructing the wavelet representation for shape learning. By truncating the SDF, regions not close to the shape surface would be cast to a constant function to make efficient the wavelet decomposition and shape

learning. Otherwise, we found that the shape learning process will collapse and the training loss cannot be reduced.

4.2 Shape Learning

Next, to learn the 3D shape distribution in a given shape set, we gather coefficient volumes $\{C_i^j, D_i^j\}$ of the shapes in the set for training (i) the *generator network* to learn to iteratively remove noise from a random Gaussian noise sample to generate C_i^J ; and (ii) the *detail predictor network* to learn to predict D_i^j from C_i^j to enhance the details in the generated shapes. Further, to enable shape inversion, we may additionally train (iii) the *encoder network* (jointly optimized with the *generator network*) to learn a latent space for mapping the coarse coefficient volume C_i^J to a latent code z_i .

Network structure. To start, we formulate a simple but efficient neural network structure for both the generator and detail predictor networks. The two networks have the same structure, as both take a 3D volume as input and output a 3D volume of the same resolution as the input. Specifically, we adopt a modified 3D version of the U-Net architecture [Nichol and Dhariwal 2021]. First, we apply three 3D residual blocks to progressively compose and downsample the input into a set of multi-scale features and a bottleneck feature volume. Then, we apply a single self-attention layer to aggregate features in the bottleneck volume, so that we can efficiently incorporate non-local information into the features. Further, we upsample and concatenate features in the same scale and progressively perform an inverse convolution with three residual blocks to produce the output. For all convolution layers in the network structure, we use a filter size of three with a stride of one.

For the encoder network, we design a five-layer 3D convolutional neural network with kernel size $k = 4$ and stride $s = 1$, each followed by an instance normalization. Also, we adopt a single linear transform to produce the output latent code z .

In the followings, we will first introduce the modeling of the shape generation process, followed by the adaptation for the shape inversion process. Lastly, we will introduce the detail predictor network for enhancing the details of the generated shapes.

Modeling the shape generation process. We formulate the 3D shape generation process based on the denoising diffusion probabilistic model [Sohl-Dickstein et al. 2015]. For simplicity, we drop the subscript and superscript in C_i^j , and denote $\{C_0, \dots, C_T\}$ as the shape generation sequence, where C_0 is the target, which is C_i^J ; C_T is a random noise volume from the Gaussian prior; and T is the total number of time steps. As shown on top of Figure 2(b), we have (i) a forward process (denoted as $q(C_{0:T})$) that progressively adds noise based on a Gaussian distribution to corrupt C_0 into a random noise volume; and (ii) a backward process (denoted as $p_\theta(C_{0:T})$) that employs the generator network (with network parameter θ) to iteratively remove noise from C_T to generate the target. Note that all 3D shapes $\{C_0, \dots, C_T\}$ are represented as 3D volumes and each voxel value is a wavelet coefficient at its spatial location.

Both the forward and backward processes are modeled as the Markov processes. The generator network is optimized to maximize the generation probability of the target, i.e., $p_\theta(C_0)$. Also, as suggested in [Ho et al. 2020], this training procedure can be further

simplified to use the generator network to predict the noise volume ϵ_θ . So, we adopt a mean-squares loss to train our framework:

$$L_2 = E_{t, C_0, \epsilon} [\|\epsilon - \epsilon_\theta(C_t, t)\|^2], \epsilon \sim \mathcal{N}(0, \mathbf{I}), \quad (1)$$

where t is the time steps; ϵ is a noise volume; and $\mathcal{N}(0, \mathbf{I})$ denotes a unit Gaussian distribution. In particular, we first sample noise volume ϵ from a unit Gaussian distribution $\mathcal{N}(0, \mathbf{I})$ and time step $t \in [1, \dots, T]$ to corrupt C_0 into C_t . Then, our generator network learns to predict noise ϵ based on the corrupted coefficient volume C_t . Further, as the network takes time step t as input, we convert value t into an embedding via two MLP layers. Using this embedding, we can condition all the convolution modules in the prediction and enable the generator to be more aware of the amount of noise contaminated in C_t . For more details on the derivation of the training objectives, please refer to supplementary material Section J.

Modeling the shape inversion process. The shape inversion process aims to embed a given 3D shape as a compact code z , such that we can faithfully reconstruct the coarse wavelet volume C_0 of the shape from z and further reconstruct the shape. Motivated by [Preechakul et al. 2022], we introduce an optional encoder Enc_ϕ to derive the latent code z of coarse wavelet volume C_0 , i.e., $z = Enc_\phi(C_0)$. Then, we inject z into the generator during the backward process as an additional shape condition; see the bottom part of Figure 2(b). During the training, we jointly optimize the encoder and generator networks to maximize the conditional generation probability, i.e., $p_\theta(C_0|z)$. This can be achieved by modifying the objective in Equation (1) into

$$L_2 = E_{t, C_0, \epsilon} [\|\epsilon - \epsilon_\theta(C_t, z, t)\|^2], \epsilon \sim \mathcal{N}(0, \mathbf{I}). \quad (2)$$

Note that since we need the generator to be aware of the current shape condition, we follow [Preechakul et al. 2022] to use the group normalization layers to jointly take the time embedding and the latent code as the input to the generator.

Detail predictor network. Next, we train the detail predictor network to produce the detail coefficient volume D_0 from coarse coefficient volume C_0 (see the top part of Figure 2(b)), so that we can further enhance the details in our generated (or inverted) shapes.

To train the detail predictor network, we leverage the paired coefficient volumes $\{C_i^J, D_i^J\}$ from the data preparation. Importantly, each detail coefficient volume D_0 should be highly correlated to its associated coarse coefficient volume C_0 . Hence, we pose detail prediction as a conditional regression on the detail coefficient volume, aiming at learning neural network function $f : C_0 \rightarrow D_0$; hence, we optimize f via a mean squared error loss. Overall, the detail predictor has the same network structure as the generator, but we include more convolution layers to accommodate the cubic growth in the number of nonzero values in the detail coefficient volume.

4.3 Shape Generation

Now, we are ready to generate 3D shapes. Figure 2(c) illustrates the shape generation procedure. First, we randomize a 3D noise volume as C_T from the standard Gaussian distribution. Then, we can employ the trained generator for T time steps to produce C_0 from C_T . This process is iterative and inter-dependent. We cannot parallelize the operations in different time steps, so leading to a very long computing time. To speed up the inference process, we adopt

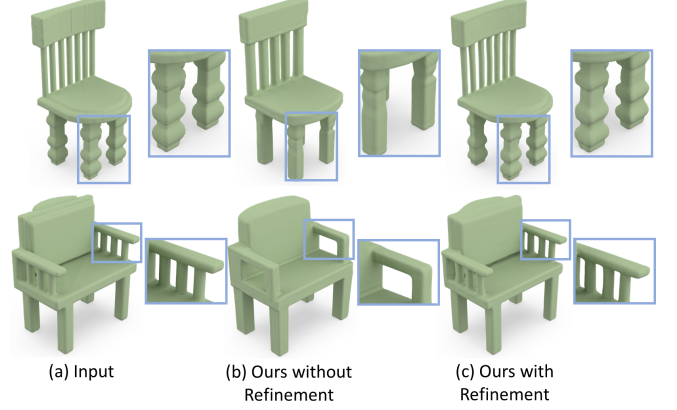


Fig. 4. Visual comparison of shape inversion with/without shape-guided refinement. Directly using our latent codes without refinement can already produce plausible shapes with overall appearance very similar to the inputs. Further refinement can enhance the reconstruction of the local structures, e.g., see the chair legs on top and the chair armrests on bottom.

an approach in [Song et al. 2020] to sub-sample a set of time steps from $[1, \dots, T]$ during the inference; in practice, we evenly sample $1/10$ of the total time steps in all our experiments.

After we obtain the coarse coefficient volume C_0 , we can then use the detail predictor network to predict the detail coefficient volume D_0 from C_0 , followed by a series of inverse wavelet transforms from $\{C_0, D_0\}$ at scale $J=3$ to reconstruct the original TSDF. By then, we can extract an explicit 3D mesh from the reconstructed TSDF using the marching cube algorithm [Lorensen and Cline 1987].

4.4 Shape Inversion

Thanks to the encoder network trained during the shape learning, our approach can leverage it for shape inversion. Having said that, our goal is to invert a given unseen shape into a latent code and then reconstruct it faithfully from the latent code.

Figure 2(d) illustrates the overall shape inversion procedure. First, we produce coarse coefficient volume C_0 from the input shape, following the procedure in Section 4.1. Then, we feed coefficient volume C_0 into the encoder network to obtain the latent code $z = Enc_\phi(C_0)$. After that, we feed latent code z together with a sampled noise volume ϵ into the generator network to directly produce a coarse coefficient volume for reproducing the original shape, following the procedure in Section 4.3.

However, directly generating the shape from latent code z would lead to loss in topological structures and fine geometric details originally in the shape; compare Figure 4(a) and (b). To enhance the quality of the inverted shape, we further propose a shape-guided refinement scheme to search for latent code z' around z in the latent space to better fit the input shape C_0 . In detail, we initialize latent code z' as z and adapt it by gradient descent using the inversion objective in Equation (2) (see Section 4.2) for 400 iterations on the input. Using the initial latent code z , we can already obtain a plausible shape similar to the input. By using this shape-guided refinement, we can further obtain fine details and structures in local regions missed in the initial code z . Also, note that during the

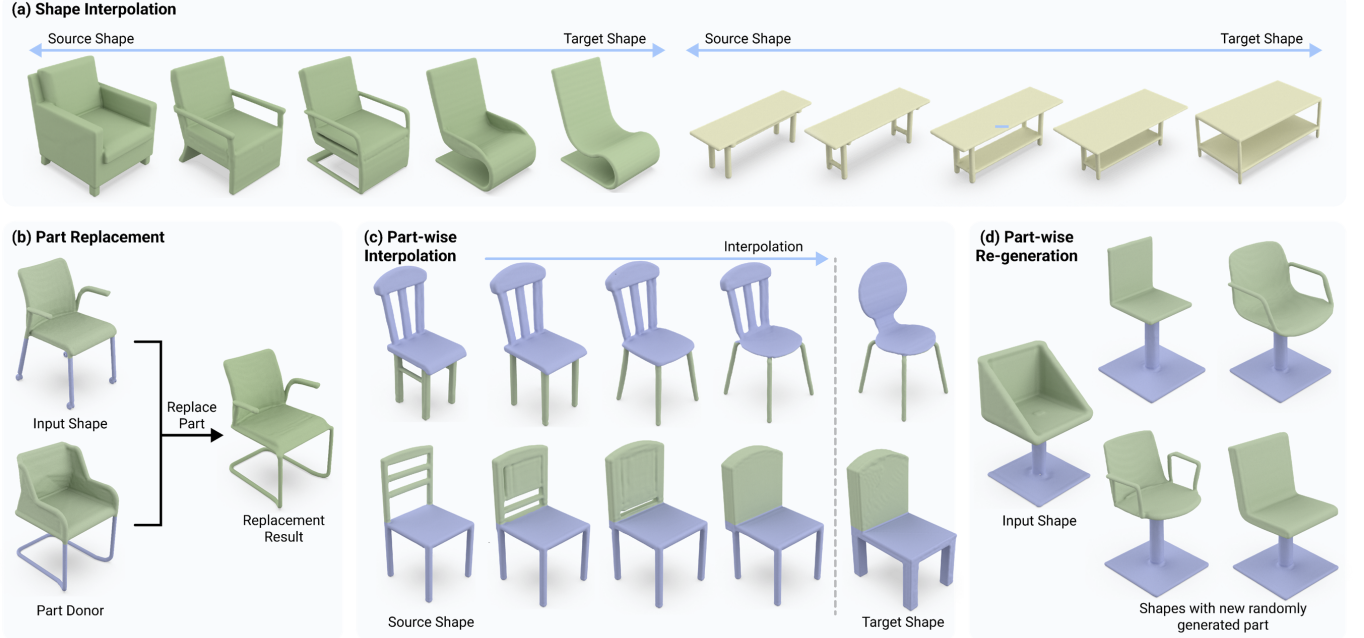


Fig. 5. Shape manipulations supported by our method. (a) Shape interpolation. We can smoothly interpolate inverted shapes to others using the learned latent space. (b) Part replacement. We can replace a part in a shape (in blue) with a part from a donor shape (in blue). (c) Part-wise shape interpolation. We can continuously interpolate only the selected part region (in green) in the source shape. (d) Part-wise shape re-generation. We can re-generate a selected part (in green) in a shape while keeping the other parts untouched (in blue). The re-generated parts are diverse, plausible, and consistent with the untouched parts.

refinement, both the encoder and generator networks are fixed. As Figure 4(c) shows, our refined latent code helps encourage more faithful shape inversion with precise topological structures and fine geometric details, more similar to the original inputs. In Section 5.2, we will present quantitative evaluation of our results, showing that our approach can produce inverted shapes of much higher fidelity, compared with the state-of-the-art methods.

4.5 Shape Manipulation

Shape inversion enables us to faithfully encode shapes into the learned latent space, in which our latent codes can faithfully represent their associated 3D shapes. Further, we design the shape generation process with the latent code as a condition. Hence, by manipulating the latent code and regenerating shape from the manipulated code, we can produce new shapes from the existing ones, e.g., by simply interpolating latent codes of different shapes; see our high-quality shape interpolation results shown in Figure 5(a).

Further than that, our method enables a rich variety of region-aware manipulations, in which we can manipulate a particular region of a shape, while leaving other regions untouched:

- (i) **Part Replacement.** First, we can replace a selected part in the input shape with a part from the donor; see Figure 5(b) for an example. Note that the new shape is still plausible and the new part is consistent with the other parts.
- (ii) **Part-wise Interpolation.** Instead of interpolating the whole shape, our method allows us to select a part in the input and

interpolate the part region towards another shape; see Figure 5(c). We can observe that changes in the selected region are smooth and semantically meaningful during the interpolation with good coherency across different parts.

- (iii) **Part-wise Re-generation.** Further, we can randomly re-generate a selected part in the input; see the upper part of the chair in Figure 5(d). Our re-generated parts are diverse, plausible, and consistent with the untouched parts.

To support these region-aware shape manipulations, we utilize the property that our generated coarse coefficient volume C_0 can maintain a good spatial correspondence with the original TSDF volume. Hence, one can select a region in a shape and locally manipulate the associated portion in the coarse coefficient volume. However, naively changing the coefficient values in the selected region will introduce noise around the connecting boundary, since the new coefficient values may not be consistent with the original coefficients in the other regions of the shape; see, e.g., Figure 7(a).

To address this issue, we propose the region-aware manipulation procedure shown in Figure 6 by extending the shape inversion pipeline. Overall, the diffusion process takes T steps to produce the manipulated coarse coefficient volume C_0^A from the random noise volume C_T^A . See Figure 6 (top left), given input shape A and its refined latent code z_A (from Section 4.4), we first run the shape inversion process for ΔT steps to obtain the partially-denoised coefficient volume $C_{T-\Delta T}^A$. In parallel, see Figure 6 (bottom left), we do the same on input shape B (which can be the donor/target shape, depending

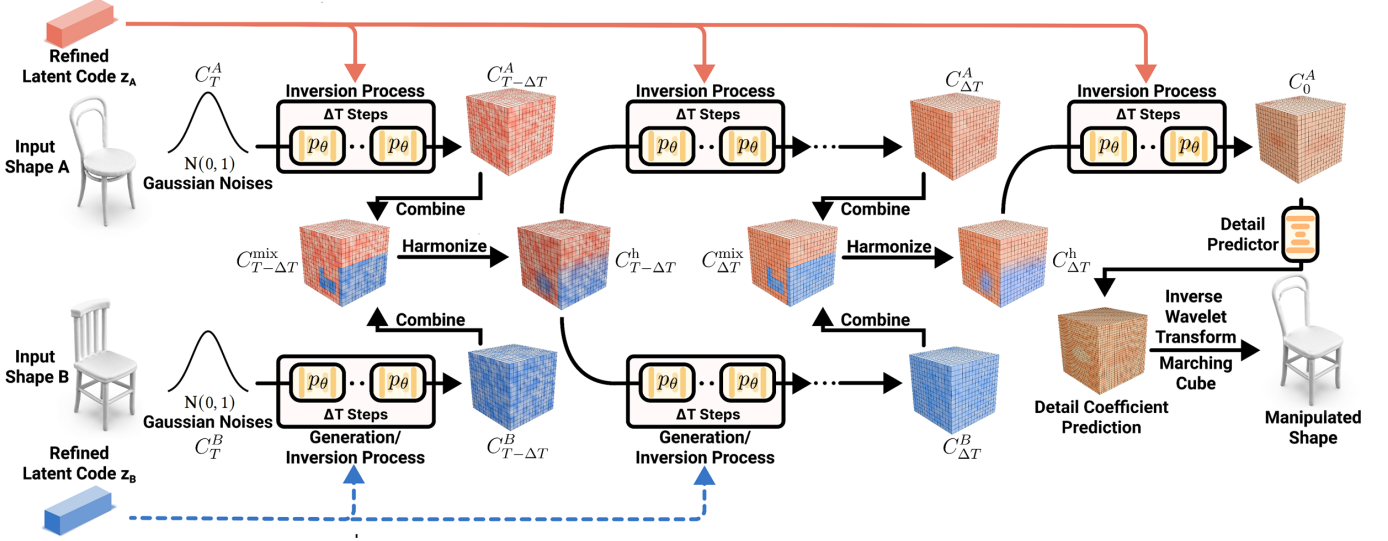


Fig. 6. Overview of our region-aware manipulation procedure, taking T steps to produce the manipulated coarse coefficient volume C_0^A from the sampled 3D Gaussian noise volume C_T^A . First, we run two inversion processes (left side) for ΔT steps in parallel, guided by the two refined latent codes z_A and z_B from input shapes A and B to produce two partially-denoised coefficient volumes $C_{T-\Delta T}^A$ and $C_{T-\Delta T}^B$, respectively. We then spatially combine the coefficient values of two coefficient volumes to obtain the mixed coefficient volume $C_{T-\Delta T}^{\text{mix}}$ and further harmonize values in the boundary regions to produce $C_{T-\Delta T}^h$. With the harmonized coefficient volume as guidance, we repeat this combine-and-harmonize process every ΔT steps until we produce the manipulated coefficient volume C_0^A . Also, we can replace the bottom inversion process with an unconditional shape generation process for achieving part-wise re-generation.

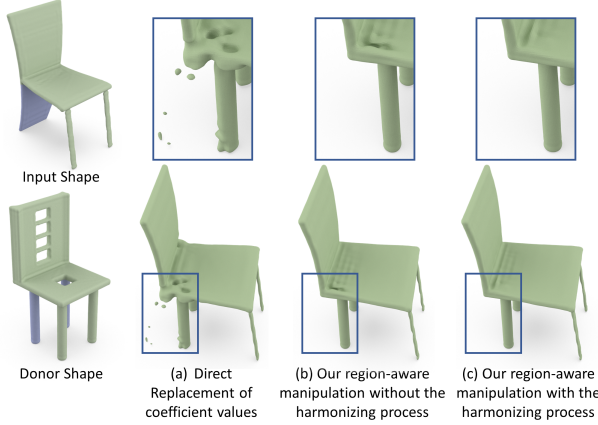


Fig. 7. Visual comparisons on part replacement by: (a) a direct replacement of coefficient values; (b) our region-aware manipulation without the harmonizing process; and (c) our full region-aware manipulation procedure with the harmonizing process. Directly replacing the coefficient values leads to noise near the boundaries between the new part from the donor shape and the remaining parts in the input shape; see (a). Without the harmonizing process, inconsistencies in the coefficient volume could introduce artifacts on the manipulated shape; see (b). With our full approach, we can smooth out the connected regions for more consistent part replacement; see (c).

on the type of the manipulation operation) and its refined code z_B to produce another coefficient volume $C_{T-\Delta T}^B$.

Importantly, after every ΔT steps in the diffusion process (where $T = M \cdot \Delta T$ for some positive integer M), we replace the coefficient

values in the selected region of $C_{T-\Delta T}^A$ by those in $C_{T-\Delta T}^B$ to produce the mixed coefficient volume $C_{T-\Delta T}^{\text{mix}}$. As the coefficient values near the mixed boundary in $C_{T-\Delta T}^{\text{mix}}$ may not be consistent from $C_{T-\Delta T}^A$ and $C_{T-\Delta T}^B$, the generated shapes may contain some small artifacts; see, e.g., Figure 7(b). To smooth the coefficient mixing, we propose to adopt the harmonizing process in [Lugmayr et al. 2022] to produce the harmonized coefficient volume $C_{T-\Delta T}^h$ (details in the next paragraph). By harmonizing $C_{T-\Delta T}^{\text{mix}}$ after combining $C_{T-\Delta T}^A$ and $C_{T-\Delta T}^B$, we can obtain a smooth transition of coefficient values near the boundary; see the improved result in Figure 7(c). After that, the harmonized coefficient volume can guide the subsequent steps of the two processes, so we use a combine-and-harmonize process in every ΔT steps to obtain the final manipulated coefficient volume; see again Figure 6. We empirically set $\Delta T = 10$ for region-aware manipulation experiments. Also, we can replace the inversion process guided by the refined latent code z_B with an unconditional shape generation for achieving part-wise re-generation. For the details on how we select the manipulation region in the input shape and how we compute the corresponding region in the wavelet domain; please refer to supplementary material Section F.

Details on the harmonizing process. Given the mixed coefficient volume C_t^{mix} , we follow the forward process of the diffusion model to add noise to it by sampling $C_{t+1}^{\text{mix}} \sim \mathcal{N}(\sqrt{1 - \beta_t}C_t, \beta_t\mathbf{I})$. Then, we apply the two inversion processes mentioned above, guided by the refined latent codes z_A and z_B , respectively, separately on C_{t+1}^{mix} , for a single step to obtain two denoised coefficient volumes. We then combine the volumes according to the selected region again and repeat the above adding noise and denoising procedure ten

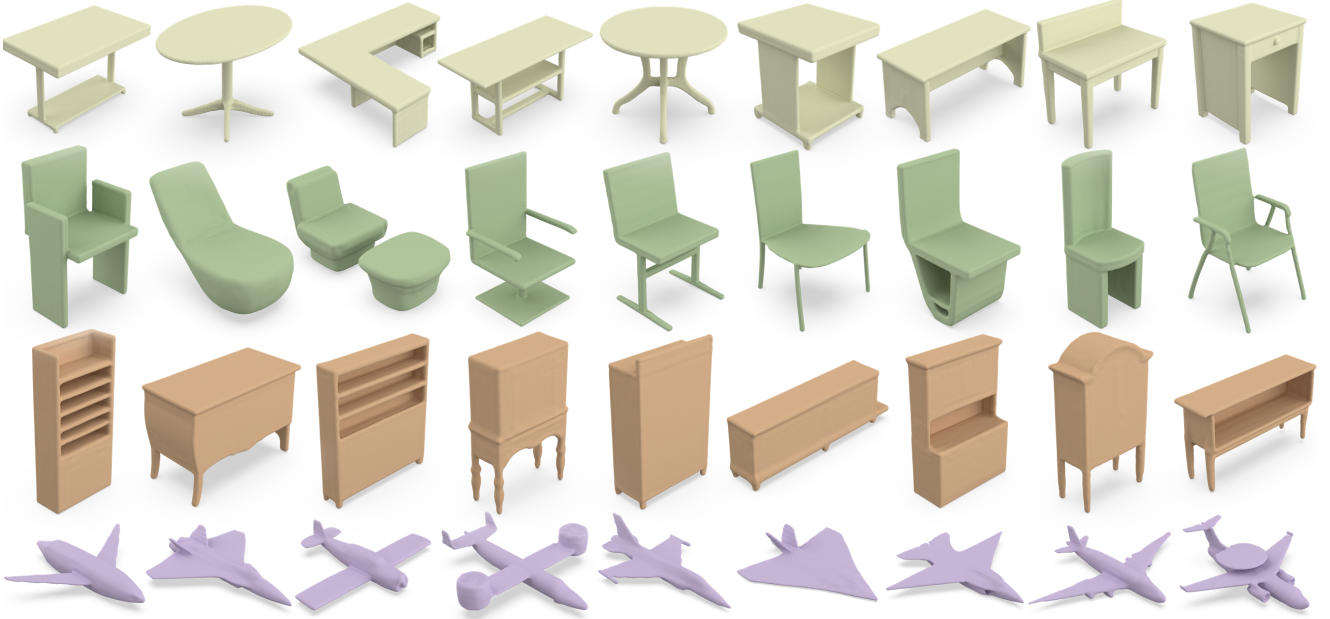


Fig. 8. Gallery of our generated shapes: Table, Chair, Cabinet, and Airplane (top to bottom). Our shapes exhibit complex structures, fine details, and clean surfaces, without obvious artifacts, compared with those generated by the other approaches; see Figure 9.

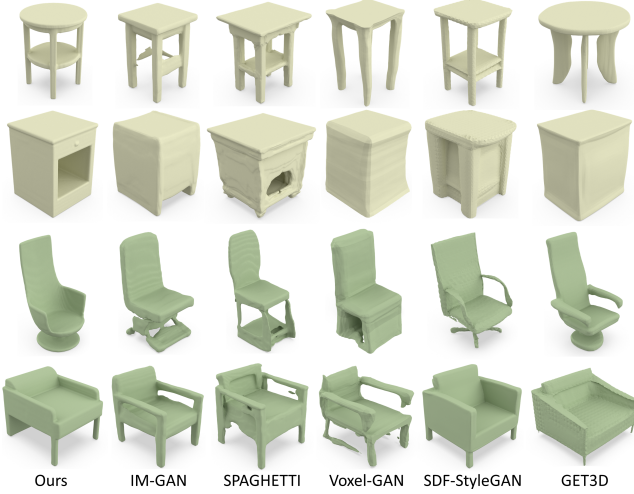


Fig. 9. Visual comparisons with state-of-the-art methods. Our generated shapes exhibit finer details and cleaner surfaces, without obvious artifacts.

times to obtain the harmonized coefficient volume. By doing so, the generator can better account for the coefficient value changes in the manipulated region and adapt the values near the boundary. In the case of part-wise re-generation, we use the unconditional shape generation for harmonizing the mixed coefficient volume instead of the inversion process guided by the refined latent code z_B .

4.6 Implementation Details

We employed ShapeNet [Chang et al. 2015] to prepare the training dataset used in all our experiments. For shape generation, we follow the data split in [Chen and Zhang 2019] and use only the training split to supervise our network training. For shape inversion, we

follow the data split in [Park et al. 2019] for ease of comparison. Also, similar to [Hertz et al. 2022; Li et al. 2021; Luo and Hu 2021], we train one model of each category in the ShapeNet dataset [Chang et al. 2015] for both shape generation and inversion.

We implement our networks using PyTorch and run all experiments on a GPU cluster with four RTX3090 GPUs. For both shape generation and inversion, we follow [Ho et al. 2020] to set $\{\beta_t\}$ to increase linearly from $1e^{-4}$ to 0.02 for 1,000 steps and set $\sigma_t = \frac{1-\alpha_t-1}{1-\alpha_t} \beta_t$. We train the generator, optionally with the encoder, for 800,000 iterations and the detail predictor for 60,000 iterations, both using the Adam optimizer [Kingma and Ba 2014] with a learning rate of $1e^{-4}$. Training the generator and detail predictor takes around three days and 12 hours, respectively. For shape-guided refinement, we also adopt Adam optimizer [Kingma and Ba 2014] with a learning rate of $5e^{-2}$ for 400 iterations. For shape generation, the inference takes around six seconds per shape on an RTX 3090 GPU. For shape inversion, the refinement procedure and inference totally take around two minutes on an RTX 3090 GPU using 1000 diffusion steps. As for shape manipulation, our region-aware manipulation procedure takes four minutes on an RTX 3090 GPU for running 1000 diffusion steps. We adapt [Cotter 2020] to implement the 3D wavelet decomposition. *We will release our code and training data upon the publication of this work.*

5 RESULTS AND EXPERIMENTS

5.1 Shape Generation

Galleries of our generated shapes. We present Figure 1 (left) and Figure 8 to showcase the compelling capability of our method for generating shapes of various categories. Our generated shapes exhibit *diverse topology*, *fine details*, and also *clean surfaces without obvious artifacts*, covering a rich variety of small, thin, and complex

Table 1. Quantitative comparison between the generated shapes produced by our method and six state-of-the-art methods. We follow the same setting to conduct this experiment as in the state-of-the-art methods. From the table, we can see that our generated shapes have the best quality for almost all cases (largest COV, lowest MMD, and 1-NNA close to 50) for both the Chair and Airplane categories. The units of CD and EMD are 10^{-3} and 10^{-2} , respectively.

Method	Chair						Airplane					
	COV \uparrow		MMD \downarrow		1-NNA ~ 50		COV \uparrow		MMD \downarrow		1-NNA ~ 50	
	CD	EMD	CD	EMD	CD	EMD	CD	EMD	CD	EMD	CD	EMD
IM-GAN [Chen and Zhang 2019]	56.49	54.50	11.79	14.52	61.98	63.45	61.55	62.79	3.320	8.371	76.21	76.08
Voxel-GAN [Kleineberg et al. 2020]	43.95	39.45	15.18	17.32	80.27	81.16	38.44	39.18	5.937	11.69	93.14	92.77
Point-Diff [Luo and Hu 2021]	51.47	55.97	12.79	16.12	61.76	63.72	60.19	62.30	3.543	9.519	74.60	72.31
SPAGHETTI [Hertz et al. 2022]	49.19	51.92	14.90	15.90	70.72	68.95	58.34	58.38	4.062	8.887	78.24	77.01
SDF-StyleGAN [Zheng et al. 2022]	51.77	50.30	13.45	15.43	68.88	70.20	57.97	48.33	3.859	9.406	83.37	84.36
GET3D [Gao et al. 2022]	53.47	56.41	14.43	15.63	70.32	69.51	55.62	55.38	4.134	9.421	89.12	86.77
Ours	58.19	55.46	11.70	14.31	61.47	61.62	64.78	64.40	3.230	7.756	71.69	66.74

structures that are typically very challenging for the existing approaches to produce. More 3D shape generation results produced by our method are provided in supplementary material Section A.

Baselines for comparison. We compare the shape generation capability of our method with six state-of-the-art methods: IM-GAN [Chen and Zhang 2019], Voxel-GAN [Kleineberg et al. 2020], Point-Diff [Luo and Hu 2021], SPAGHETTI [Hertz et al. 2022], SDF-StyleGAN [Zheng et al. 2022], and GET3D [Gao et al. 2022]. To our best knowledge, our method is the first work that generates implicit shape representations in frequency domain and considers coarse and detail coefficients to enhance the generation of structures and fine details.

Our experiments follow the same setting as the above works. Specifically, we leverage our trained model on the Chair and Airplane categories in ShapeNet [Chang et al. 2015] to randomly generate 2,000 shapes for each category. Then, we uniformly sample 2,048 points on each generated shape and evaluate the shapes using the same set of metrics as in the previous methods (details to be presented later). For GET3D, we use the official pre-trained model for the Chair category and adopt their code to train a model for the Airplane category, which is not provided in their released repository. For the other comparison methods, we employ publicly-released trained network models to generate shapes.

Evaluation metrics for shape generation. Following [Hertz et al. 2022; Luo and Hu 2021], we evaluate the generation quality using (i) minimum matching distance (MMD) measures the fidelity of the generated shapes; (ii) coverage (COV) indicates how well the generated shapes cover the given 3D repository; and (iii) 1-NN classifier accuracy (1-NNA) measures how well a classifier differentiates the generated shapes from those in the repository. Overall, a low MMD, a high COV, and an 1-NNA close to 50% indicate good generation quality; see supplementary material Section K for the details.

Quantitative evaluation for shape generation. Table 1 reports the quantitative comparison results, showing that our method surpasses all others for almost all the evaluation cases over the three metrics for both the Chair and Airplane categories. We employ the Chair category, due to its large variations in structure and topology, and the Airplane category, due to the fine details in its shapes. As discussed in [Luo and Hu 2021; Yang et al. 2019], the COV and MMD metrics have limited capabilities to account for details, so they are not suitable for measuring the fine quality of the generation results, e.g., the

generated shapes sometimes show a better performance even when compared with the ground-truth training shapes on these metrics. In contrast, 1-NNA is more robust and can better correlate with the generation quality. In this metric, our approach outperforms all others, while having a significant margin in the Airplane category, manifesting the diversity and fidelity of our generated results.

Qualitative evaluation for shape generation. Figure 9 shows some visual comparisons. For each random shape generated by our method, we find a similar shape (with similar structures and topology) generated by each of the other methods to make the visual comparison easier. See supplementary material Sections B and D for more visual comparisons. Further, as different methods likely have different statistical modes in the generation distribution, we also take random shapes generated by IM-GAN and find similar shapes generated by our method for comparison; see supplementary material Section C for the results. From all these results, we can see that the 3D shapes generated by our method clearly exhibit finer details, higher fidelity structures, and cleaner surfaces, without obvious artifacts.

5.2 Shape Inversion

Baselines for comparison. We compare our shape inversion results with those from four state-of-the-art methods: IM-NET [Chen and Zhang 2019], DeepSDF [Park et al. 2019], DualSDF [Hao et al. 2020], and SPAGHETTI [Hertz et al. 2022]. We employ their official code to train their models, following the same train-test split as [Park et al. 2019] for a fair comparison. Note that we do not evaluate the results of SPAGHETTI in the Lamp category, as its official pre-trained model is unavailable and the training code has not been officially released by the time of the submission. Further, we notice a very recent work, NeuForm [Lin et al. 2022], which overfits the given shape for achieving the shape inversion. Even though the code and pre-trained models of this work have not been released, we provide a visual comparison on the inversion results in supplementary material Section E using the example results given in their paper.

Evaluation metrics for shape inversion. Following prior works, we evaluate the inversion quality by measuring the similarity between the inverted shapes and the original inputs using Chamfer Distance (CD), Earth Mover’s Distance (EMD), and Light Field Distance (LFD) [Chen et al. 2003]. For CD and EMD, they evaluate point-wise distances between two point clouds sampled on the shape surfaces. Here, we uniformly sample 2048 points on each shape (inverted and

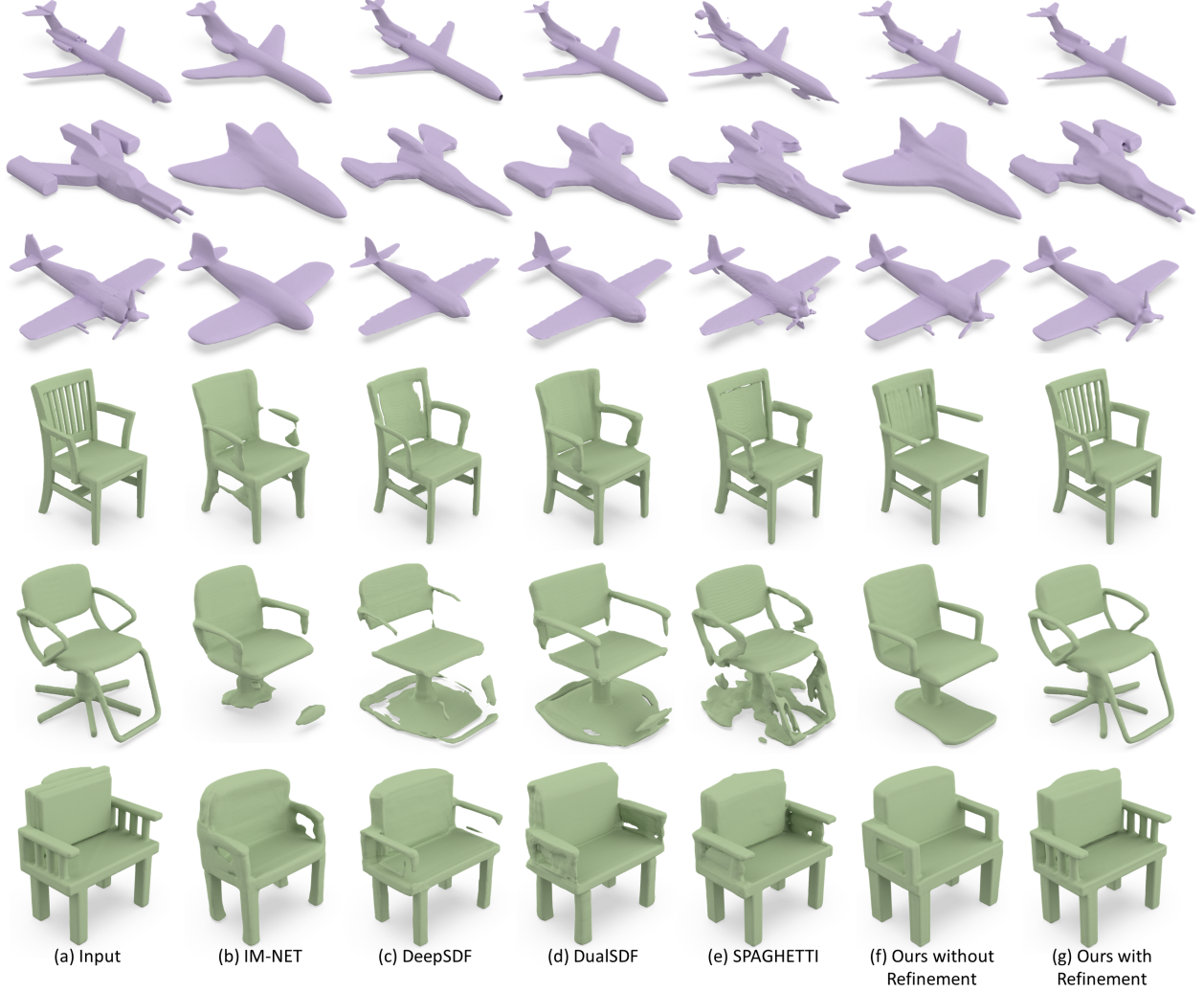


Fig. 10. Visual comparisons on shape inversion. Our method is able to produce more faithful inverted shapes (g) that are highly similar to the inputs (a), compared with others (b-e). Our inverted results exhibit fine details and complete structures; see, *e.g.*, the chair pulleys and airplane propellers, which are typically very challenging for the existing methods (b-e). Also, our method, without further refinements (f), can still produce reasonable shape inversions.

original) and evaluate the metrics on the sampled point clouds. For LFD, it measures the difference between two shapes in the rendered image domain. First, we uniformly sample 20 viewpoints to render images for each of the inverted shapes and input shapes. Then, we compute a 45-dimension feature vector for each rendered image and obtain the final metric by summing up all pairwise L1 distances between the image feature vectors from the same viewpoint. Note that a low value indicates a better performance for all three metrics. Also, there could be noise in the sampled TSDF grid, so we post-process the inverted shapes. For the details on the metrics and post-processing, please see supplementary material Section L.

Quantitative evaluation for shape inversion. Table 2 shows the quantitative comparison results. Without refinement, our method already performs better in all metrics than IM-NET [Chen and Zhang 2019], which also does not require additional refinement. By further refining the latent code, our method can significantly outperform

all the other methods in all metrics. Particularly, for the LFD metric, our method manifests more than 30% performance gain over the second-best method in all categories.

Qualitative evaluation for shape inversion. Figure 10 shows some visual comparisons on shape inversion. We can observe that our method can already produce plausible results without refinement; see Figure 10(f). By further introducing the shape-guided refinement, we can faithfully reproduce the fine details and complex structures in the input shapes; see, *e.g.*, the thin structures at the chair’s back and the aircraft’s propeller shown in the third and fourth rows of Figure 10; they cannot be achieved by the existing works.

5.3 Shape Manipulation

Shape Interpolation. As Figure 11 shows, our method can produce smooth and plausible interpolations between two unseen shapes, thanks to the shape-guided refinement. From left to right, the source

Table 2. Quantitative comparison on shape inversion between our method and four state-of-the-art methods. We follow the same setting as in the state-of-the-art methods. Our method outperforms (lowest CD, EMD, and LFD) all the other methods for all categories. The units of CD, EMD, and LFD are 10^{-3} , 10^{-2} , and 1, respectively. Notice that the quantitative evaluation for SPAGHETTI [Hertz et al. 2022] in the Lamp category is not shown here, as SPAGHETTI does not provide the pre-trained model of Lamp and the training code has not been officially released.

Method	Chair			Airplane			Lamp		
	CD ↓	EMD ↓	LFD ↓	CD ↓	EMD ↓	LFD ↓	CD ↓	EMD ↓	LFD ↓
IM-NET [Chen and Zhang 2019]	4.968	10.42	2800.56	3.301	9.261	5024.65	20.253	20.403	6880.01
DeepSDF [Kleineberg et al. 2020]	4.657	9.066	2403.08	3.249	9.734	4939.56	17.540	18.918	6858.34
DualSDF [Luo and Hu 2021]	8.254	13.01	2588.87	6.529	15.74	7097.09	35.125	26.692	6820.62
SPAGHETTI [Hertz et al. 2022]	2.837	7.663	1988.82	1.386	6.466	3637.33	—	—	—
Ours without Refinement	4.578	8.919	2358.98	2.459	6.816	3726.43	17.412	19.237	6955.02
Ours	1.142	4.491	924.911	1.108	4.507	2508.55	5.834	7.201	3450.34



Fig. 11. High-quality shapes created by interpolating our refined latent codes. Note the smooth transition from the sources to the targets. Particularly, the intermediate shapes are mostly plausible with fine details.

can morph smoothly towards the target; see especially the consistent changes in the armrests in the last row of Figure 11. These results manifest the superior capability of our framework to embed an unseen shape in a smooth and plausible latent space.

Part Replacement. Besides, we can select a part in an input shape and replace it with a corresponding part in the donor shape. As Figure 12 shows, we replace the blue part in each input (a) with the blue part in the corresponding donor (b) to generate new shapes (d). Note that the new shapes exhibit high fidelity, while preserving the geometric details of (a) & (b). See particularly the last row of Figure 12; the complex armrests and back in the input shape can be well preserved in our new shape, while the chair’s seat and legs are seamlessly connected with clean surfaces and sharp edges.

Further, we compare our method with SPAGHETTI [Hertz et al. 2022], the state-of-the-art implicit method for the same task. In particular, SPAGHETTI produces inverted shapes as a mixture of Gaussian distributions, where each of them is conditioned by a latent code. Part replacement on the input can then be conducted by replacing some particular latent codes with the corresponding ones in another shape. However, their results are somehow noisy in the connecting regions, while struggling to preserve the geometry and details of the input and part donor; see Figure 12 (c). More visual comparisons on part replacement with SPAGHETTI [Hertz et al. 2022] and COALESCE [Kangxue Yin and Zhang 2020] are provided



Fig. 12. Part replacement results. We replace the blue part in the original shape (a) with the blue part in the donor shape (b), thus generating new shapes (d). Compared with SPAGHETTI (c), our method can better preserve the original parts, e.g., legs and castors, and produce plausible shapes.

in supplementary material Section F. Note also that for the examples shown in the main paper, we cannot provide comparisons of COALESCE, since it needs additional part-level annotations, which are not available for these examples.

Part-wise Interpolation. Also, our method enables us to select a part (region) in the source shape and perform interpolation on it towards the target shape. See, e.g., Figure 13; during the interpolation, the green part of the source morphs smoothly towards the associated part in the target shape while preserving the remaining parts (marked in blue). See the drawer’s knobs of the table in the

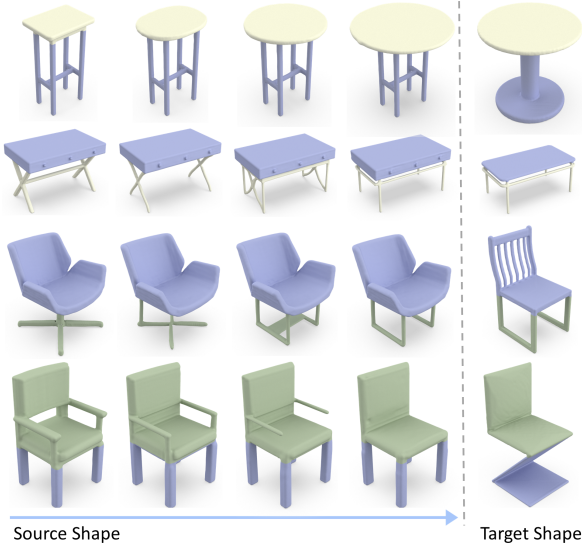


Fig. 13. Part-wise interpolation results. Our method can interpolate the selected part (yellow for the tables and green for the chairs) in the sources (leftmost) towards the targets (rightmost). As shown, the intermediate results morph smoothly on the selected region, while preserving other parts.

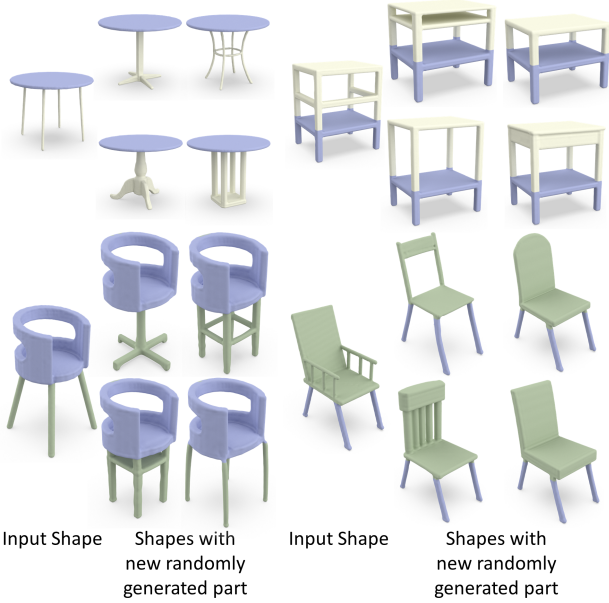


Fig. 14. Part-wise re-generation results. We keep the blue parts fixed and randomly re-generate the remaining parts. Note the diverse structures and geometries in the re-generated parts. See the chair at bottom right; new parts replace the original back and its seat can exhibit various styles, e.g., one with vertical bars and the other with a round back. Also, the geometries of the legs are consistent across the results.

second row and the chair’s legs in the third row of Figure 13, the geometry and topology of the untouched parts are preserved faithfully. Besides, the selected part of the intermediate results is consistent with the untouched part; see the connecting regions between the chair’s seat and legs in the last row of Figure 13.

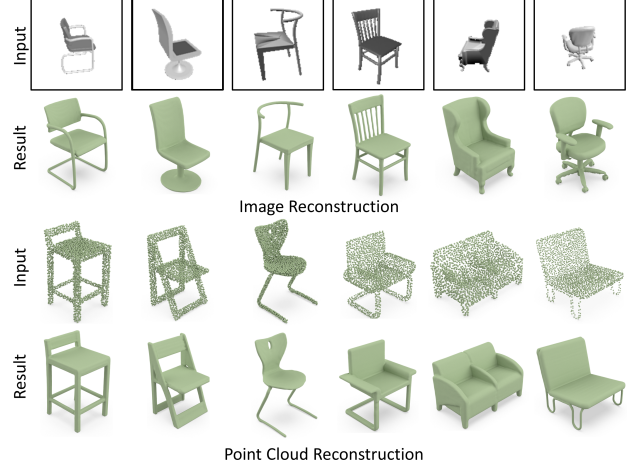


Fig. 15. Shape reconstruction results. Our method can embed single-view images (top) and point clouds (bottom) into our latent space and faithfully reconstruct shapes that match the raw inputs. Note the complex topology structures and fine geometric details in the reconstructed shapes.

Part-wise Re-generation. Further, our method allows us to specify a part in the input shape and replace it with a randomly-generated part; see Figure 14. The randomly-generated parts are diverse and plausible; see the table at top left of Figure 14. The connecting regions in the tables keep consistent across all the re-generation results, while the re-generated legs of the tables exhibit diverse topology structures and geometric details.

More shape manipulation results. Please refer to supplementary material Section F for more results on shape interpolation, part replacement, part-wise interpolation, and part-wise re-generation.

5.4 Shape Reconstruction

Shape reconstruction from point clouds and single-view images. By utilizing the latent space learned by the encoder network, we can leverage our method to help reconstruct implicit shapes from various forms of inputs. As suggested by [Chen and Zhang 2019], we propose to train another encoder that takes a point cloud or a single-view image as input and to predict a latent code that matches the one obtained by our trained encoder network in Section 4.2. Given an unseen input (a point cloud or a single-view image), we can then use the new encoder to generate a corresponding latent code and take the code to reconstruct the 3D shape.

Figure 15 shows visual examples of our reconstruction results. We can reconstruct shapes with fine details and thin structures solely by predicting the latent codes. The results show that the learned latent space is highly smooth and covers various unseen inputs. Interestingly, our method can reconstruct some occluded parts in the single-view images, e.g., the occluded legs of the chairs, by leveraging the shape priors learned in the latent space.

5.5 Novelty analysis on Shape Generation

Next, we analyze whether our method can generate shapes that are not necessarily the same as the training-set shapes, meaning that it does not simply memorize the training data. To do so, we use our method to generate 500 random shapes and retrieve top-four

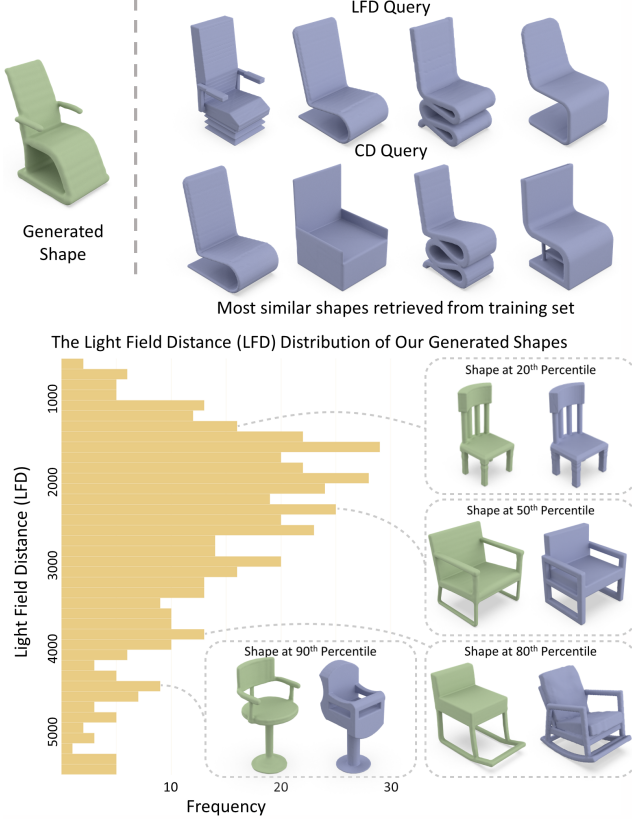


Fig. 16. Shape novelty analysis. Top: From our generated shape (in green), we retrieve top-four most similar shapes (in blue) in training set by CD and LFD. Bottom: We generate 500 chairs using our method; for each chair, we retrieve the most similar shape in the training set by LFD; then, we plot the distribution of LFDs for all retrievals, showing that our method is able to generate shapes that are more similar (low LFDs) or more novel (high LFDs) compared to the training set. Note that the generated shape at 50th percentile is already not that similar to the associated training-set shape.

most similar shapes in the training set separately via two different metrics, *i.e.*, Chamfer Distance (CD) and Light Field Distance (LFD) [Chen et al. 2003]. It is noted that LFD is computed based on rendered images from multiple views on each shape, so it focuses more on the visual similarity between shapes and is considered to be more robust for shape retrieval. For the details on the metrics, please see supplementary material Section H.

Figure 16 (top) shows a shape generated by our method, together with top-four most similar shapes retrieved from the training set by the CD and LFD metrics. Further, we show another ten examples in supplementary material Section G. Comparing our shapes with the retrieved ones, we can see that the shapes share similar structures, showing that our method is able to generate realistic-looking structures like those in the training set. Beyond that, our shapes exhibit noticeable differences in various local structures.

As mentioned earlier, a good generator should produce diverse shapes that are not necessarily the same as the training shapes. So, we further statistically analyze the novelty of our generated shapes relative to the training set. To do so, we use our method to generate

Table 3. Comparing our full generation pipeline with various ablated cases on the Chair category. The unit of CD is 10^{-3} and the unit of EMD is 10^{-2} .

Method	COV \uparrow		MMD \downarrow		1-NNA ~ 50	
	CD	EMD	CD	EMD	CD	EMD
Full Model	58.19	55.46	11.70	14.31	61.47	61.62
W/o detail predictor	54.20	50.96	12.32	14.54	62.46	62.57
VAD Generator	21.83	26.77	21.83	26.77	95.20	93.62
Direct predict TSDF	50.51	50.67	12.83	15.24	68.69	68.29

Table 4. Comparing our full inversion pipeline with various ablated cases on the Chair category. The units of CD, EMD, and LFD are 10^{-3} , 10^{-2} , and 1, respectively.

Method	CD \downarrow	EMD \downarrow	LFD \downarrow
Full Model	1.142	4.491	924.91
W/o Refinement	4.578	8.919	2358.98
W/o detail predictor	1.194	5.129	1200.04

500 random chairs; for each generated chair shape, we use LFD to retrieve the most similar shape in the training set. Figure 16 (bottom) plots the distribution of LFDs between our generated shapes (in green) and retrieved shapes (in blue). Also, we show four shape pairs at various percentiles, revealing that shapes with larger LFDs are more different from the most similar shapes in the training set. From the LFD distribution, we can see that our method can learn a generation distribution that covers shapes in the training set (low LFD) and also generates novel and realistic-looking shapes that are more different (high LFD) from the training-set shapes.

5.6 Ablation Study

Ablation on shape generation. To evaluate the major components in shape generation, we successively ablate its full pipeline. First, we evaluate the generation performance with/without the detail predictor. Next, we study the contributions of the diffusion model and the wavelet representation in the generator network.

From the results reported in Table 2, we can see the capability of the detail predictor, which introduces a substantial improvement on all metrics (first vs. second rows). Further, replacing our generator with the VAD model or directly predicting TSDF leads to a performance degradation (second & last two rows).

Ablation on shape inversion. Next, we explore our shape inversion pipeline on the Chair category to evaluate its major components. First, we quantitatively evaluate the effect of directly reconstructing the input from the latent code predicted by the encoder without the shape-guided refinement. Second, we evaluate the shape inversion performance with/without the detail predictor. Table 4 reports the quantitative results, demonstrating the capability of shape-guided refinement (first vs. second rows). Further, dropping the detail predictor degrades the performance (first vs. third rows).

Details of ablation study. Please refer to supplementary material Section M for details on how the ablation cases are implemented and visual comparison results on shape generation and inversion.

5.7 Limitations and Future works.

Discussion on shape generation. While our method can generate diverse and realistic-looking shapes, the generated shapes may not



Fig. 17. Failure cases. Left: chairs that are unlikely to meet the basic functionality in real world. Right: artifacts in complex and very thin structures.

meet the desired functionality. As Figure 17(a) shows, the generated chairs, despite looking interesting and structurally reasonable, have an exceptionally tall seat back and low seat height for normal human bodies. In the future, we may incorporate functionality, e.g., [Blinn et al. 2021], into the shape generation process. Second, though our method can learn efficiently via the wavelet representation, it still requires a large number of shapes for training. So, for categories with few training samples, especially those with complex and very thin structures; see, e.g., Figure 17(b), the generated shape may exhibit artifacts like broken parts and structures. Last, while our method can better fit the data distribution than existing methods, the generated shapes still conform to structures/appearances in the training set. Exploring how to generate out-of-distribution shapes is an interesting but challenging future direction.

Discussion on shape inversion and manipulation. Our method is able to invert and reconstruct shapes faithfully and facilitate manipulations with high fidelity, yet requiring users to manually select regions for manipulation. An interesting future direction is to guide the shape manipulation by sketches or texts [Li et al. 2017a; Liu et al. 2022]. Also, while our compact wavelet representation maintains a good spatial correspondence with the original TSDF domain and enables various part-aware manipulations, inter-shape correspondences still rely mainly on a canonically-aligned dataset. We hope to establish stronger correspondences in the compact wavelet domain to enable more compelling downstream applications such as texture and detail transfer. Besides, the diffusion process requires a large number of time steps, so producing manipulated shapes is time-consuming. Yet, simply reducing the time steps leads to a significant quality drop. We plan to explore acceleration strategies to promote interactive shape manipulation.

6 CONCLUSION

This paper presents a new framework for 3D shape generation, inversion, and manipulation. Unlike prior works, we operate on the frequency domain. By decomposing the implicit function in the form of the TSDF using biorthogonal wavelets, we build a compact wavelet representation with a pair of coarse and detail coefficient volumes, as an encoding of 3D shape. Then, we formulate our generator upon a probabilistic diffusion model to learn to generate diverse shapes in the form of coarse coefficient volumes from noise samples and a detail predictor to further learn to generate compatible detail coefficient volumes for reconstructing fine details. Further, by introducing an encoder into the generation process, our framework

can enable faithful inversion of unseen shapes, shape interpolation, and a rich variety of region-aware manipulations. Both quantitative and qualitative experiments show superior capabilities of our new approach on shape generation, inversion, and manipulation over the state-of-the-art methods.

REFERENCES

- Rameen Abdal, Peihao Zhu, Niloy J. Mitra, and Peter Wonka. 2021. StyleFlow: Attribute-conditioned exploration of StyleGAN-generated images using conditional continuous normalizing flows. *ACM Transactions on Graphics (SIGGRAPH)* 40, 3 (2021), 1–21.
- Panos Achlioptas, Olga Diamanti, Ioannis Mitliagkas, and Leonidas J. Guibas. 2018. Learning representations and generative models for 3D point clouds. In *Proceedings of International Conference on Machine Learning (ICML)*. 40–49.
- Matan Atzmon and Yaron Lipman. 2020. SAL: Sign agnostic learning of shapes from raw data. In *IEEE Conference on Computer Vision and Pattern Recognition (CVPR)*. 2565–2574.
- David Bau, Hendrik Strobel, William Peebles, Jonas Wulff, Bolei Zhou, Jun-Yan Zhu, and Antonio Torralba. 2019. Semantic Photo Manipulation with a Generative Image Prior. *ACM Transactions on Graphics (SIGGRAPH)* 38, 4 (2019), 11.
- Bryce Blinn, Alexander Ding, Daniel Ritchie, R. Kenny Jones, Srinath Sridhar, and Manolis Savva. 2021. Learning Body-Aware 3D Shape Generative Models. *arXiv preprint arXiv:2112.07022* (2021).
- Ruojin Cai, Guandao Yang, Hadar Averbuch-Elor, Zekun Hao, Serge Belongie, Noah Snaveley, and Bharath Hariharan. 2020. Learning gradient fields for shape generation. In *European Conference on Computer Vision (ECCV)*. 364–381.
- Angel X. Chang, Thomas Funkhouser, Leonidas J. Guibas, Pat Hanrahan, Qixing Huang, Zimo Li, Silvio Savarese, Manolis Savva, Shuran Song, Hao Su, et al. 2015. ShapeNet: An information-rich 3D model repository. *arXiv preprint arXiv:1512.03012* (2015).
- Ding-Yun Chen, Xiao-Pei Tian, Yu-Te Shen, and Ming Ouhyoung. 2003. On visual similarity based 3D model retrieval. In *Computer Graphics Forum*, Vol. 22. 223–232.
- Zhiqin Chen and Hao Zhang. 2019. Learning implicit fields for generative shape modeling. In *IEEE Conference on Computer Vision and Pattern Recognition (CVPR)*. 5939–5948.
- Zhang Chen, Yinda Zhang, Kyle Genova, Sean Fanello, Sofien Bouaziz, Christian Häne, Ruofei Du, Cem Keskin, Thomas Funkhouser, and Danhang Tang. 2021. Multiresolution Deep Implicit Functions for 3D Shape Representation. In *IEEE International Conference on Computer Vision (ICCV)*. 13087–13096.
- Julian Chibane, Thiemo Alldieck, and Gerard Pons-Moll. 2020. Implicit functions in feature space for 3D shape reconstruction and completion. In *IEEE Conference on Computer Vision and Pattern Recognition (CVPR)*. 6970–6981.
- Albert Cohen. 1992. Biorthogonal wavelets. *Wavelets: A Tutorial in Theory and Applications* 2 (1992), 123–152.
- Fergal Cotter. 2020. *Uses of Complex Wavelets in Deep Convolutional Neural Networks*. Ph.D. Dissertation. University of Cambridge.
- Ingrid Daubechies. 1990. The wavelet transform, time-frequency localization and signal analysis. *IEEE transactions on information theory* 36, 5 (1990), 961–1005.
- Prafulla Dhariwal and Alexander Nichol. 2021. Diffusion models beat GANs on image synthesis. *Conference on Neural Information Processing Systems (NeurIPS)* (2021), 8780–8794.
- Haoqiang Fan, Hao Su, and Leonidas J. Guibas. 2017. A point set generation network for 3D object reconstruction from a single image. In *IEEE Conference on Computer Vision and Pattern Recognition (CVPR)*. 605–613.
- Rizal Fathony, Anit Kumar Sahu, Devin Willmott, and J. Zico Kolter. 2020. Multiplicative filter networks. In *International Conference on Learning Representations (ICLR)*.
- Rinon Gal, Amit Bermano, Hao Zhang, and Daniel Cohen-Or. 2020. MRGAN: Multi-Rooted 3D Shape Generation with Unsupervised Part Disentanglement. In *IEEE International Conference on Computer Vision (ICCV)*. 2039–2048.
- Jun Gao, Tianchang Shen, Zian Wang, Wenzheng Chen, Kangxue Yin, Daiqing Li, Or Litany, Zan Gojcic, and Sanja Fidler. 2022. GET3D: A Generative Model of High Quality 3D Textured Shapes Learned from Images. In *Conference on Neural Information Processing Systems (NeurIPS)*.
- Kyle Genova, Forrester Cole, Avneesh Sud, Aaron Sarna, and Thomas Funkhouser. 2020. Local deep implicit functions for 3D shape. In *IEEE Conference on Computer Vision and Pattern Recognition (CVPR)*. 4857–4866.
- Rohit Girdhar, David F. Fouhey, Mikel Rodriguez, and Abhinav Gupta. 2016. Learning a predictable and generative vector representation for objects. In *European Conference on Computer Vision (ECCV)*. 484–499.
- Amos Gropp, Lior Yariv, Niv Haim, Matan Atzmon, and Yaron Lipman. 2020. Implicit geometric regularization for learning shapes. In *Proceedings of International Conference on Machine Learning (ICML)*. 3569–3579.
- Thibault Groueix, Matthew Fisher, Vladimir G. Kim, Bryan C. Russell, and Mathieu Aubry. 2018. A papier-mâché approach to learning 3D surface generation. In *IEEE Conference on Computer Vision and Pattern Recognition (CVPR)*. 216–224.

- Zekun Hao, Hadar Averbuch-Elor, Noah Snaveley, and Serge Belongie. 2020. DualSDF: Semantic shape manipulation using a two-level representation. In *IEEE Conference on Computer Vision and Pattern Recognition (CVPR)*. 7631–7641.
- Amir Hertz, Or Perel, Raja Giryes, Olga Sorkine-Hornung, and Daniel Cohen-Or. 2022. SPAGHETTI: Editing Implicit Shapes Through Part Aware Generation. *ACM Transactions on Graphics (SIGGRAPH)* 41, 4 (2022), 20.
- Jonathan Ho, Ajay Jain, and Pieter Abbeel. 2020. Denoising diffusion probabilistic models. *Conference on Neural Information Processing Systems (NeurIPS)* (2020), 6840–6851.
- Ka-Hei Hui, Ruihui Li, Jingyu Hu, and Chi-Wing Fu. 2022. Neural wavelet-domain diffusion for 3D shape generation. In *Proceedings of SIGGRAPH ASIA*. 9.
- Ka-Hei Hui*, Ruihui Li*, Jingyu Hu, and Chi-Wing Fu (* joint first authors). 2022. Neural Template: Topology-aware Reconstruction and Disentangled Generation of 3D Meshes. In *IEEE Conference on Computer Vision and Pattern Recognition (CVPR)*.
- Le Hui, Rui Xu, Jin Xie, Jianjun Qian, and Jian Yang. 2020. Progressive point cloud deconvolution generation network. In *European Conference on Computer Vision (ECCV)*. 397–413.
- Moritz Ibing, Isaak Lim, and Leif Kobbelt. 2021. 3D Shape Generation With Grid-Based Implicit Functions. In *IEEE Conference on Computer Vision and Pattern Recognition (CVPR)*. 13559–13568.
- Li Jiang, Shaoshuai Shi, Xiaojuan Qi, and Jiaya Jia. 2018. GAL: Geometric adversarial loss for single-view 3D-object reconstruction. In *European Conference on Computer Vision (ECCV)*. 802–816.
- Siddhartha Chaudhuri Matthew Fisher Vladimir Kim Kangxue Yin, Zhiqin Chen and Hao Zhang. 2020. COALESCE: Component Assembly by Learning to Synthesize Connections. In *International Conference on 3D Vision (3DV)*.
- Hyeongju Kim, Hyeonseung Lee, Woo Hyun Kang, Joun Yeop Lee, and Nam Soo Kim. 2020. SoftFlow: Probabilistic framework for normalizing flow on manifolds. In *Conference on Neural Information Processing Systems (NeurIPS)*. 16388–16397.
- Diederik P. Kingma and Jimmy Ba. 2014. Adam: A method for stochastic optimization. *arXiv preprint arXiv:1412.6980* (2014).
- Marian Kleineberg, Matthias Fey, and Frank Weichert. 2020. Adversarial generation of continuous implicit shape representations. In *Eurographics (short paper)*.
- Changjian Li, Hao Pan, Yang Liu, Xin Tong, Alla Sheffer, and Wenping Wang. 2017a. Bendsketch: Modeling freeform surfaces through 2D sketching. *ACM Transactions on Graphics (SIGGRAPH)* 36, 4 (2017), 1–14.
- Jun Li, Kai Xu, Siddhartha Chaudhuri, Ersin Yumer, Hao Zhang, and Leonidas J. Guibas. 2017b. GRASS: Generative recursive autoencoders for shape structures. *ACM Transactions on Graphics (SIGGRAPH)* 36, 4 (2017), 1–14.
- Manyi Li and Hao Zhang. 2021. D²IM-Net: Learning detail disentangled implicit fields from single images. In *IEEE Conference on Computer Vision and Pattern Recognition (CVPR)*. 10246–10255.
- Ruihui Li, Xianzhi Li, Ke-Hei Hui, and Chi-Wing Fu. 2021. SP-GAN: Sphere-Guided 3D Shape Generation and Manipulation. *ACM Transactions on Graphics (SIGGRAPH)* 40, 4 (2021).
- Connor Z. Lin, Niloy J. Mitra, Gordon Wetzstein, Leonidas Guibas, and Paul Guerrero. 2022. NeuForm: Adaptive Overfitting for Neural Shape Editing. In *Conference on Neural Information Processing Systems (NeurIPS)*.
- Lingjie Liu, Jiatao Gu, Kyaw Zaw Lin, Tat-Seng Chua, and Christian Theobalt. 2020. Neural sparse voxel fields. *Conference on Neural Information Processing Systems (NeurIPS)* (2020), 15651–15663.
- Shichen Liu, Shunsuke Saito, Weikai Chen, and Hao Li. 2019. Learning to infer implicit surfaces without 3D supervision. *Conference on Neural Information Processing Systems (NeurIPS)* (2019), 12.
- Shi-Lin Liu, Hao-Xiang Guo, Hao Pan, Pengshuai Wang, Xin Tong, and Yang Liu. 2021. Deep Implicit Moving Least-Squares Functions for 3D Reconstruction. In *IEEE Conference on Computer Vision and Pattern Recognition (CVPR)*. 1788–1797.
- Zhengzhe Liu, Yi Wang, Xiaojuan Qi, and Chi-Wing Fu. 2022. Towards Implicit Text-Guided 3D Shape Generation. In *IEEE Conference on Computer Vision and Pattern Recognition (CVPR)*. 17896–17906.
- William E. Lorensen and Harvey E. Cline. 1987. Marching Cubes: A high resolution 3D surface construction algorithm. In *Proceedings of SIGGRAPH*, Vol. 21. 163–169.
- Andreas Lugmayr, Martin Danelljan, Andres Romero, Fisher Yu, Radu Timofte, and Luc Van Gool. 2022. Repaint: Inpainting using denoising diffusion probabilistic models. In *IEEE Conference on Computer Vision and Pattern Recognition (CVPR)*. 11461–11471.
- Andrew Luo, Tianqin Li, Wen-Hao Zhang, and Tai Sing Lee. 2021. SurfGen: Adversarial 3D Shape Synthesis with Explicit Surface Discriminators. In *IEEE International Conference on Computer Vision (ICCV)*. 16238–16248.
- Shitong Luo and Wei Hu. 2021. Diffusion probabilistic models for 3D point cloud generation. In *IEEE Conference on Computer Vision and Pattern Recognition (CVPR)*. 2837–2845.
- Stephane G. Mallat. 1989. A theory for multiresolution signal decomposition: the wavelet representation. *IEEE transactions on pattern analysis and machine intelligence* 11, 7 (1989), 674–693.
- Julien N. P. Martel, David B. Lindell, Connor Z. Lin, Eric R. Chan, Marco Monteiro, and Gordon Wetzstein. 2021. ACORN: Adaptive coordinate networks for neural scene representation. *ACM Transactions on Graphics (SIGGRAPH)* 40, 4 (2021), 13.
- Lars Mescheder, Michael Oechsle, Michael Niemeyer, Sebastian Nowozin, and Andreas Geiger. 2019. Occupancy networks: Learning 3D reconstruction in function space. In *IEEE Conference on Computer Vision and Pattern Recognition (CVPR)*. 4460–4470.
- Kaichun Mo, Paul Guerrero, Li Yi, Hao Su, Peter Wonka, Niloy J. Mitra, and Leonidas J. Guibas. 2019. StructureNet: Hierarchical graph networks for 3D shape generation. *ACM Transactions on Graphics (SIGGRAPH Asia)* 38, 6 (2019), 242:1–242:19.
- Alexander Quinn Nichol and Prafulla Dhariwal. 2021. Improved denoising diffusion probabilistic models. In *Proceedings of International Conference on Machine Learning (ICML)*. 8162–8171.
- Michael Niemeyer, Lars Mescheder, Michael Oechsle, and Andreas Geiger. 2020. Differentiable volumetric rendering: Learning implicit 3D representations without 3D supervision. In *IEEE Conference on Computer Vision and Pattern Recognition (CVPR)*. 3504–3515.
- Jeong Joon Park, Peter Florence, Julian Straub, Richard Newcombe, and Steven Lovegrove. 2019. DeepSDF: Learning continuous signed distance functions for shape representation. In *IEEE Conference on Computer Vision and Pattern Recognition (CVPR)*. 165–174.
- Konpat Preechakul, Nattanat Chatthee, Suttisak Wizadwongsa, and Supasorn Suwajanakorn. 2022. Diffusion autoencoders: Toward a meaningful and decodable representation. In *IEEE Conference on Computer Vision and Pattern Recognition (CVPR)*. 10619–10629.
- Vishwanath Saragam, Jasper Tan, Guha Balakrishnan, Richard G. Baraniuk, and Ashok Veeraraghavan. 2022. MINER: Multiscale Implicit Neural Representations. In *European Conference on Computer Vision (ECCV)*.
- Edward J. Smith, Scott Fujimoto, Adriana Romero, and David Meger. 2019. GEOMETrics: Exploiting geometric structure for graph-encoded objects. In *Proceedings of International Conference on Machine Learning (ICML)*. 5866–5876.
- Edward J. Smith and David Meger. 2017. Improved adversarial systems for 3D object generation and reconstruction. In *Conference on Robot Learning*. PMLR, 87–96.
- Jascha Sohl-Dickstein, Eric Weiss, Niru Maheswaranathan, and Surya Ganguli. 2015. Deep unsupervised learning using nonequilibrium thermodynamics. In *Proceedings of International Conference on Machine Learning (ICML)*. 2256–2265.
- Jiaming Song, Chenlin Meng, and Stefano Ermon. 2020. Denoising diffusion implicit models. *arXiv preprint arXiv:2010.02502* (2020).
- Towaki Takikawa, Joey Litalien, Kangxue Yin, Karsten Kreis, Charles Loop, Derek Nowrouzezahrai, Alec Jacobson, Morgan McGuire, and Sanja Fidler. 2021. Neural geometric level of detail: Real-time rendering with implicit 3D shapes. In *IEEE Conference on Computer Vision and Pattern Recognition (CVPR)*. 11358–11367.
- Jiapeng Tang, Xiaoguang Han, Junyi Pan, Kui Jia, and Xin Tong. 2019. A skeleton-bridged deep learning approach for generating meshes of complex topologies from single RGB images. In *IEEE Conference on Computer Vision and Pattern Recognition (CVPR)*. 4541–4550.
- Jiapeng Tang, Xiaoguang Han, Mingkui Tan, Xin Tong, and Kui Jia. 2021. SkeletonNet: A topology-preserving solution for learning mesh reconstruction of object surfaces from RGB images. *IEEE Transactions Pattern Analysis & Machine Intelligence* 44, 10 (2021), 6454–6471.
- Ayush Tewari, Mohamed Elgharib, Florian Bernard, Hans-Peter Seidel, Patrick Pérez, Michael Zollhöfer, and Christian Theobalt. 2020. PIE: Portrait image embedding for semantic control. *ACM Transactions on Graphics (SIGGRAPH Asia)* 39, 6 (2020), 1–14.
- Omer Tov, Yuval Alaluf, Yotam Nitzan, Or Patashnik, and Daniel Cohen-Or. 2021. Designing an encoder for StyleGAN image manipulation. *ACM Transactions on Graphics (SIGGRAPH)* 40, 4 (2021), 1–14.
- Luiz Velho, Demetri Terzopoulos, and Jonas Gomes. 1994. Multiscale implicit models. In *Proceedings of SIGGRAPH*, Vol. 94. 93–100.
- Nanyang Wang, Yinda Zhang, Zhuwen Li, Yanwei Fu, Wei Liu, and Yu-Gang Jiang. 2018. Pixel2Mesh: Generating 3D mesh models from single RGB images. In *European Conference on Computer Vision (ECCV)*. 52–67.
- Fangyin Wei, Elena Sizikova, Avneesh Sud, Szymon Rusinkiewicz, and Thomas Funkhouser. 2020. Learning to infer semantic parameters for 3D shape editing. In *2020 International Conference on 3D Vision (3DV)*. 434–442.
- Jiajun Wu, Chengkai Zhang, Tianfan Xue, Bill Freeman, and Josh Tenenbaum. 2016. Learning a probabilistic latent space of object shapes via 3D generative-adversarial modeling. In *Conference on Neural Information Processing Systems (NeurIPS)*. 82–90.
- Weihao Xia, Yulun Zhang, Yujia Yang, Jing-Hao Xue, Bolei Zhou, and Ming-Hsuan Yang. 2022. Gan inversion: A survey. *IEEE Transactions Pattern Analysis & Machine Intelligence* (2022).
- Qiangeng Xu, Weiyue Wang, Duygu Ceylan, Radomir Mech, and Ulrich Neumann. 2019. DISN: Deep implicit surface network for high-quality single-view 3D reconstruction. In *Conference on Neural Information Processing Systems (NeurIPS)*. 490–500.
- Yifan Xu, Tianqi Fan, Yi Yuan, and Gurprit Singh. 2020. Ladybird: Quasi-Monte Carlo sampling for deep implicit field based 3D reconstruction with symmetry. In *European Conference on Computer Vision (ECCV)*. 248–263.
- Xingguang Yan, Liqiang Lin, Niloy J. Mitra, Dani Lischinski, Daniel Cohen-Or, and Hui Huang. 2022. ShapeFormer: Transformer-based shape completion via sparse

- representation. In *IEEE Conference on Computer Vision and Pattern Recognition (CVPR)*. 6239–6249.
- Guandao Yang, Yin Cui, Serge Belongie, and Bharath Hariharan. 2018. Learning single-view 3D reconstruction with limited pose supervision. In *European Conference on Computer Vision (ECCV)*. 86–101.
- Guandao Yang, Xun Huang, Zekun Hao, Ming-Yu Liu, Serge Belongie, and Bharath Hariharan. 2019. PointFlow: 3D point cloud generation with continuous normalizing flows. In *IEEE International Conference on Computer Vision (ICCV)*. 4541–4550.
- Junzhe Zhang, Xinyi Chen, Zhongang Cai, Liang Pan, Haiyu Zhao, Shuai Yi, Chai Kiat Yeo, Bo Dai, and Chen Change Loy. 2021. Unsupervised 3D shape completion through gan inversion. In *IEEE Conference on Computer Vision and Pattern Recognition (CVPR)*. 1768–1777.
- Wenbin Zhao, Jiabao Lei, Yuxin Wen, Jianguo Zhang, and Kui Jia. 2021. Sign-Agnostic Implicit Learning of Surface Self-Similarities for Shape Modeling and Reconstruction from Raw Point Clouds. In *IEEE Conference on Computer Vision and Pattern Recognition (CVPR)*. 10256–10265.
- Xin-Yang Zheng, Yang Liu, Peng-Shuai Wang, and Xin Tong. 2022. SDF-StyleGAN: Implicit SDF-Based StyleGAN for 3D Shape Generation. In *Eurographics Symposium on Geometry Processing (SGP)*.
- Linqi Zhou, Yilun Du, and Jiajun Wu. 2021. 3D shape generation and completion through point-voxel diffusion. In *IEEE International Conference on Computer Vision (ICCV)*. 5826–5835.
- Jun-Yan Zhu, Philipp Krähenbühl, Eli Shechtman, and Alexei A. Efros. 2016. Generative visual manipulation on the natural image manifold. In *European Conference on Computer Vision (ECCV)*. 597–613.
- Rui Zhu, Hamed Kiani Galoogahi, Chaoyang Wang, and Simon Lucey. 2017. Rethinking Reprojection: Closing the loop for pose-aware shape reconstruction from a single image. In *IEEE International Conference on Computer Vision (ICCV)*. 57–65.